
Supplementary information

Sedimentary basins reduce stability of Antarctic ice streams through groundwater feedbacks

In the format provided by the authors and unedited

Supplement to:

Sedimentary basins reduce stability of Antarctic ice streams through groundwater feedbacks

Lu Li^{1*}, Alan R.A. Aitken^{1,2}, Mark D. Lindsay^{1,3,4}, Bernd Kulessa^{5,6}

1 – School of Earth Sciences, The University Of Western Australia, Perth, Western Australia, 6009, Australia

2 – The Australian Centre for Excellence in Antarctic Science, The University of Western Australia, Perth, Western Australia, 6009, Australia

3 – CSIRO Mineral Resources, Perth, Western Australia, 6151, Australia

4 – ARC Industrial Transformation and Training Centre in Data Analytics for Resources and the Environment (DARE)

5 – School of Biosciences, Geography and Physics, Swansea University, Wales, SA2 8PP, UK

6 – School of Geography, Planning, and Spatial Sciences, University of Tasmania, Hobart, Tasmania, 7001, Australia

Correspondence: Lu Li (lu.li@research.uwa.edu.au)

This document includes:

1	Sedimentary basin mapping with Random Forest prediction	3
1.1	Workflow.....	3
1.2	Training points.....	3
1.2.1	Outcrop.....	4
1.2.2	Seismic observation	5
1.2.3	Potential field interpretation	6
1.3	Input features.....	7
1.3.1	Bed topography	10
1.3.2	Gravity field	13
1.3.3	Magnetic field	15
1.3.4	Cryosphere and Solid-Earth Structure	17
1.4	Methods	17
1.4.1	Input feature processing.....	17
1.4.2	Input feature reduction	18
1.4.3	Training Point Sampling	19
1.4.4	RF Model training	20
1.4.5	Accuracy measurement	20
1.5	Result.....	22
1.5.1	Input feature selection	22
1.5.2	Model tuning	24
1.5.3	Model accuracy and uncertainties.....	25
1.5.4	Input feature importance	31
1.5.5	Sensitivity test.....	32
1.6	Model limitation and robustness	33
1.6.1	Uncertainty in training point calibration.....	33
1.6.2	Uncertainty in input features.....	34
1.6.3	Model robustness	34
2	Hydro-mechanical model	36
2.1	Method.....	36
2.1.1	Geomechanical Modelling	36
2.1.2	Ice Sheet Evolution	36
2.1.3	Hydrology modelling.....	37
2.2	Model setting and boundary conditions	38
2.3	Discussion	40
2.3.1	Impact of permeability to basal water flux	40
2.3.2	Impact of sedimentary basin thickness to basal water flux	42
2.3.3	Impact of basal heat flux due to water transportation.....	43

1 Sedimentary basin mapping using Random Forest

We use a supervised machine learning method Random Forest (RF) to build a geological classification model (sedimentary basin or basement) with a consistent data-based rule. The analysis is performed in R 4.0.2 in R-Studio 1.3.1073. The code for building RF model is documented in https://github.com/LL-Geo/ANT_SEDI.

1.1 Workflow

The general workflow for building a spatial classification model in RF involves five main steps (Fig. S1): 1) training information generation, 2) input feature selection, 3) model training, 4) model prediction, and 5) model evaluation.

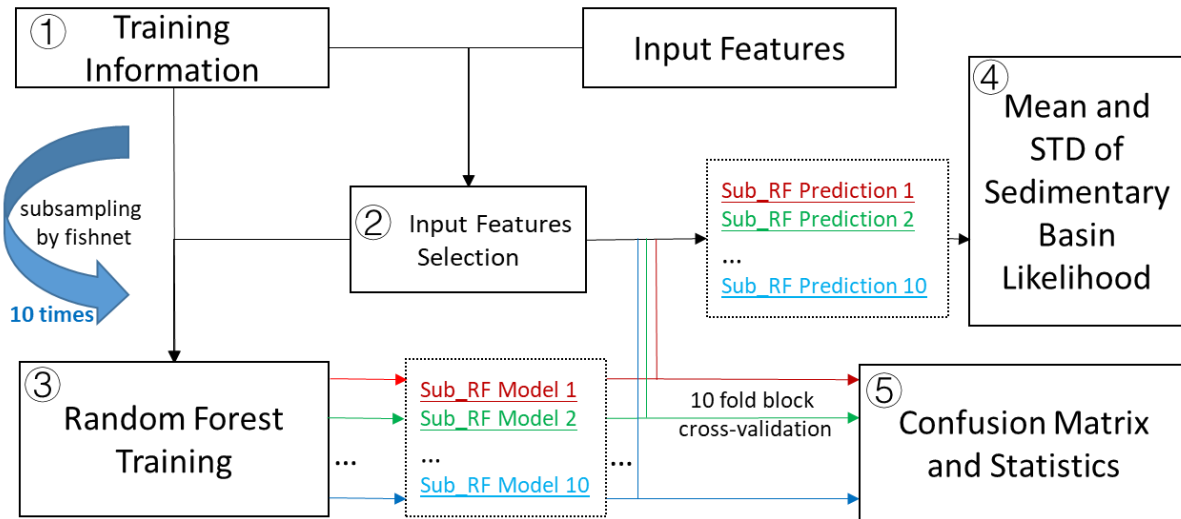


Fig. S1. Workflow in building Random Forest classification in this study.

1.2 Training points

In this study, we calibrate the model based on different observations, including bedrock outcrop, seismic measurement, and geophysical data interpretations. Each type of data has unique uncertainties due to the different methods used in each observation.

In general, we define a sedimentary basin as an accommodation space into which sediments have been deposited. In practical terms, this is defined in a subglacial setting from the geophysical detection of a substantial sedimentary accumulation. The sediments may be lithified to rock but without significant reworking and tectonic deformation. We label pre-Jurassic sedimentary outcrops as basement, as these rocks are most likely to have been uplifted, deformed or metamorphosed during the breakup of Gondwana. Typical examples include the Beacon Supergroup in the Transantarctic Mountains and the Cambrian sedimentary rocks in the Ellsworth-Whitmore Mountains. The geological setting and geophysical properties of these outcrops are not indicative of the basin-forming environment. Thus they are combined as basement class.

1.2.1 Outcrop

Due to thick ice coverage on the whole continent, rock outcrops are very sparse. We use the results derived from Geomap⁵⁵ to represent the location and type of rock outcrop. Cenozoic and Mesozoic sedimentary rocks are marked as the modern sedimentary basins found in Victoria Land and eastern Antarctic Peninsula. The Beacon Supergroup and Late Palaeozoic sedimentary rocks are marked as ancient sedimentary basins. The Beacon Supergroup sedimentary rocks are mainly distributed in the Transantarctic Mountains. The late Palaeozoic sedimentary rocks are found in Antarctic Peninsula. We label the remaining outcrops as basement, including granite, volcanic, and metamorphosed. We further merge ancient sedimentary basins as basement, because they do not represent the original basin setting and are deformed or metamorphosed. For instance, Cambrian sedimentary rock in the Ellsworth-Whitmore Mountains has formed as the basement for post-Jurassic sediment accumulation⁵⁶.

The outcrop information may introduce sample noise due to variable geology within a small area. To reduce this uncertainty, we apply 20 times a 3*3 averaging filter to the outcrop information in a 250 m cell size. This result is an outcrop geology map with a minimum spatial dimension of 10 km. We then regrid this map into a 10 km cell size. In each cell, the total likelihood of all geological units remains at 1. We keep the geology class with a likelihood larger than 0.9 for the following training process.

1.2.2 Seismic observation

Active seismic reflection and refraction methods are powerful methods to image upper crustal structures beneath ice and ocean. The major active Antarctic seismic observation is located at the continental margin recorded by Antarctic Seismic Data Library System (SDLS). In West Antarctica, Trey, et al.⁵⁷ found thick sedimentary basins in the Ross Sea area using a wide-angle reflection/refraction profile. In Weddell Sea, the seismic study showed massive sedimentary deposits up to 13 km thick under the Filchner-Ronne Ice shelf⁵⁸. Combining and interpolating the SDLS data, the GlobSed model revealed the latest total sedimentary basin thickness in offshore area⁵⁹. Here, we select the total sediment thickness > 1000 m and within the 20 km of the SDLS data to represent the offshore sedimentary basin. We define basement class where GlobSed model has sediment thickness < 1 m within the SDLS measurement range. These major basement classes are located in Pine Island Bay, and the Gunnerus Ridge in the Riiser-Larsen Sea. This basement zone in Pine Island Bay is also identified by the morphology using bathymetry data^{60,61}. However, Gohl, et al.⁶² interpreted a broader basement zone based on magnetic data. This basement zone overlaps with the sedimentary basin identified by GlobSed. We remove this overlap area in our training data as it acts as an outlier for RF classification. In Ross Sea, we limit the sedimentary basin training information within the major deposition centre. For instance, Central High and Columnan High have sediment cover, but they are not sedimentary basins in geological setting⁶³.

Over the onshore area, the combined seismic reflection and refraction experiment on Siple Coast revealed continuous and thick sedimentary basins are located at the onset area of ice stream^{64,65}. Seismic imaging also helps to constrain both soft sediment and consolidated sedimentary rocks at the bottom of Lake Vostok⁶⁶.

Besides using active seismic reflection/refraction profiles to study the subglacial geology, the passive seismic data also helps image the velocity structure (see Table. S1 for the details of the seismic station locations). Receiver function studies revealed subglacial sedimentary basin distribution in West Antarctica Rift System⁶⁷⁻⁶⁹, which is usually less than 1 km. In East Antarctica, major receiver function

study focused on the Wilkes Subglacial Basin. In the north Wilkes Subglacial Basin, a 200 to 400 m thick sediment was found at WISE station near the Eastern Basin⁷⁰. Further south, Chai, et al. ⁷¹ found a low P wave velocity structure, indicating a low density feature beneath E028 station. In south Wilkes Subglacial Basin, studies using grid search⁶⁸ and horizontal-to-vertical spectral ratio method⁷² showed sediment deposited beneath N052 and N060, respectively. Anandakrishnan and Winberry⁶⁸ found a sedimentary feature in the SPA seismic station by receiver function study at the South Pole. In central DML, Gupta, et al.⁷³ found a 1.5 km sediment beneath the ice sheet. We classify these locations as sedimentary basins except where their thickness error is larger than the estimated sediment thickness (ST09, ST13, KOLR, SIPL)⁶⁷. For the basement class, it is assigned where a low velocity sediment layer is unnecessary in the inversion. In this case, a two-layer structure including ice and crystalline crust could fit the observed receiver well⁶⁷⁻⁶⁹.

As the receiver function study uses the azimuth effect of surrounding receivers, the estimated sedimentary basin or basement structure is a regional effect. We set a 25 km radius buffer zone to receiver function locations in our training information.

1.2.3 Potential field interpretation

Topography, gravity and magnetic data are used for interpreting subglacial sedimentary basin distribution where seismic imaging is not available. Gravity and magnetic studies inferred marine and rift sediments deposited in West Antarctica. Studinger, et al.⁷⁴ evaluated regional blanketing marine sediments and linear fault-bounded sedimentary basins by isostatic adjusted topography, free-air gravity and Bouguer gravity studies over Ross ice streams. In the Interior Ross Embayment, Bell, et al.⁷⁵ found three sedimentary basins deeper than 3.6 km according to depth to magnetic source modelling. The Ellsworth–Whitmore Mountains area preserves thick Cambrian sedimentary rock up to 13 km⁵⁶. These sedimentary rocks were reworked and now form the basement for the post-Jurassic sediment⁵⁶. Subglacial sediments are also found in the interior of East Antarctica. In Coats Land, Bamber, et al.⁷⁶ reported a 3 km deep subglacial basin in Slessor half-graben using 2D Werner deconvolution depth estimation. In Wilkes Land, a deep magnetic basement structure indicates thick sedimentary rock infill⁷⁷.

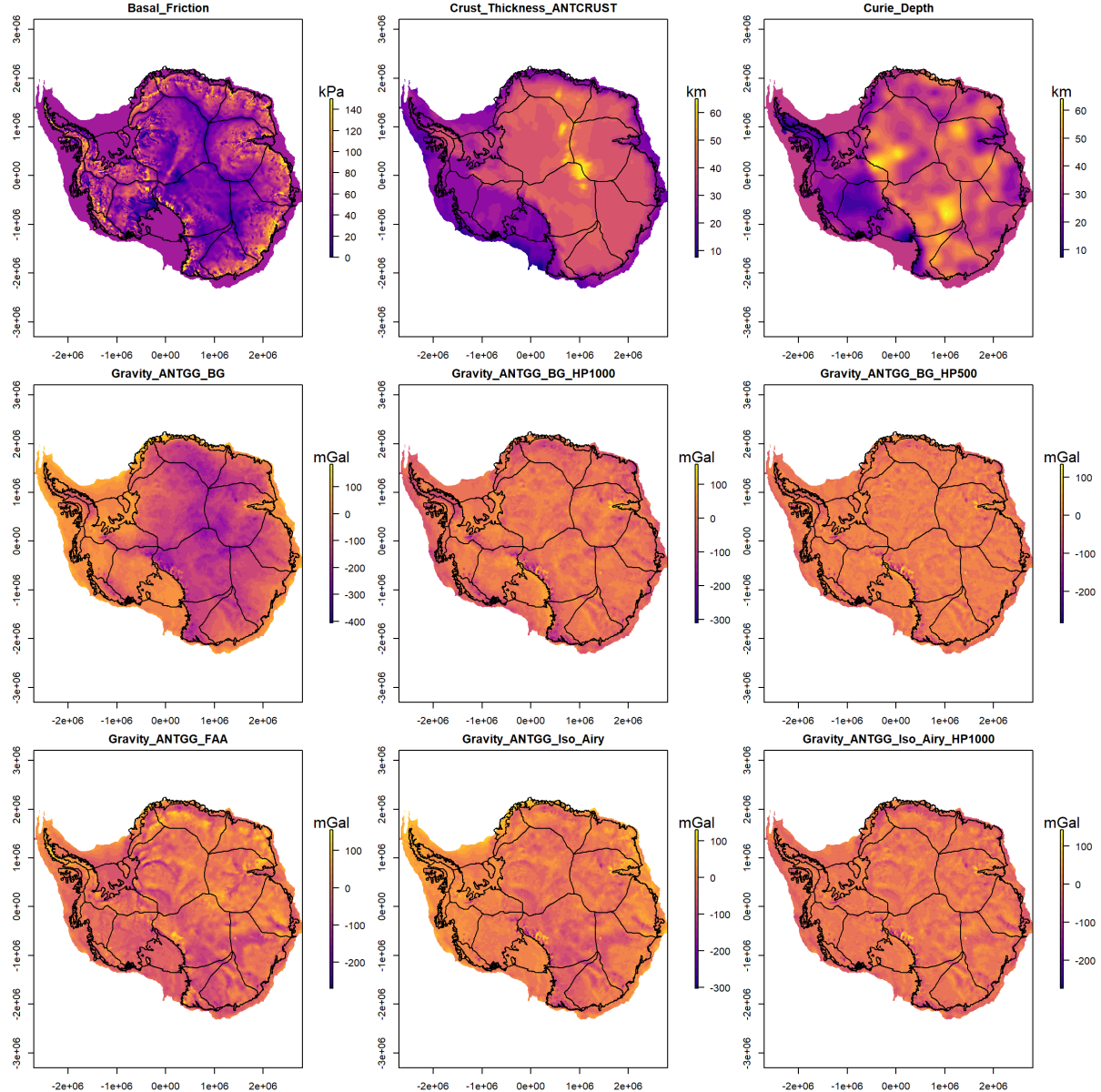
Furthermore, the variation of sediment thickness by gravity inversion in the Sabrina Subglacial Basin indicates the dynamic retreat and advance of the East Antarctic Ice-sheet¹⁵. In northern Wilkes Subglacial Basin, the high-frequency short-wavelength magnetic signature indicates the Ferrar rock pervasively intrudes Beacon sandstone⁷⁸. The negative magnetic field is interpreted as fault bounded sedimentary basins in the central Wilkes Subglacial Basin and western Wilkes Subglacial Basin, and Ross Orogen metasediment in eastern Wilkes Subglacial Basin⁷⁸. The gravity inversion of sediment thickness constrained by magnetic depth to basement suggests that the southern Wilkes Subglacial Basin has an average sediment thickness of 1623 m and the northern Wilkes Subglacial Basin has an average sediment thickness of 1144 m⁷⁹. Recently, the newly collected PolarGAP data revealed sediment fill in Pensacola Pole Basin⁸⁰.

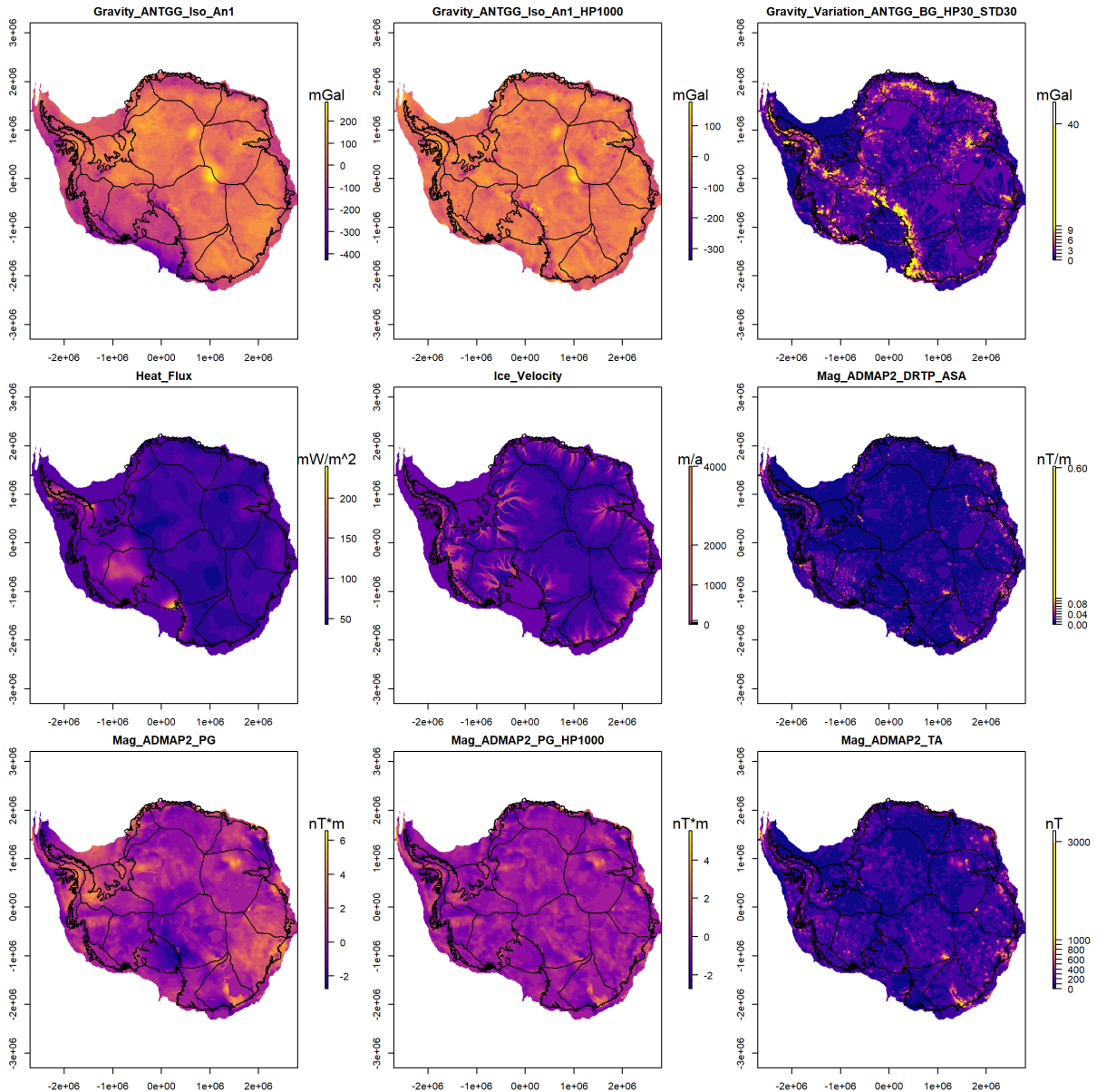
We draw the polygon of the above-mentioned sedimentary basins as inferred sedimentary basins, including Onset Basin, Offset Basin, Trunk D Basin at Siple Coast, Aurora Basin, Sabrina Basin at Wilkes Land, Wilkes Land Subglacial Basin and Pensacola Pole Basin. For the basement area, we mark the pre-Jurassic sedimentary basin in the Ellsworth-Whitmore Mountains as the basement rock⁵⁶. In Siple Coast, we label the shallow magnetic basement (< 2.5 km below sea level) as the volcanic basement^{22,75}. These shallow magnetic basement structures are interpreted as volcanioclastic rocks which are difficult to erode^{22,75}. We further mark the inferred basement in Wilkes Subglacial Basin and Wilkes Land based on integration of aerogeophysics studies^{15,79,81}. These areas mark with neglectable sediment thickness (<300 meters) from gravity inversion^{15,79,81}, which is within the unsolvable thickness bound based on gravity data and not indicative of the basin-forming environment. We also mark several deep magnetic provinces as basement, which lack of a negative isostatic gravity response⁷⁷.

1.3 Input features

We introduce input features for RF classification based on the current understanding of subglacial sedimentary basin signature. Sedimentary basin is indicated by a smooth topography surface, low residual gravity, and a deeper depth to magnetic basement, based on the sedimentary basin study in the training point generation. Low free-air gravity signals are interpreted to be low density sedimentary

rocks that infill topographic lows. We use bed elevation, gravity field, and magnetic field to represent solid-earth properties of sedimentary basin and basement.





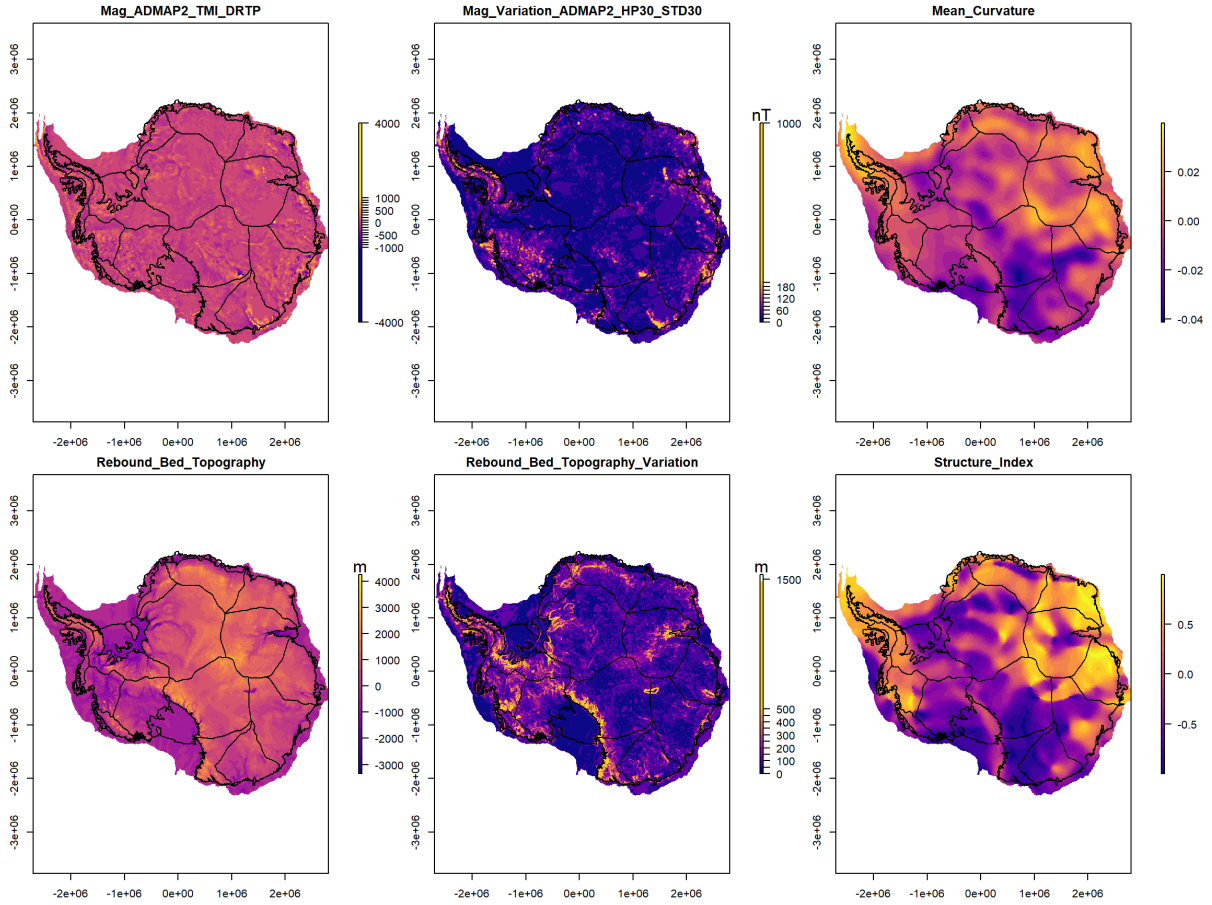


Fig S2. Input features used in this study. All evidence features are gridded into a 10 km cell size with the same extents. For the bed topography, gravity, and magnetic variation dataset, area without real measurement and associated with large uncertainty is masked and replaced by its global mean value. TMI (total magnetic intensity), DRTP (Differential reduction to the pole), HP (High-Pass filter), STD, (Standard Deviation), PG (Pseudo-Gravity), FAA (Free-Air gravity Anomaly), BG (Bouguer Gravity), Iso (Isostatic gravity).

1.3.1 Bed topography

1.3.1.1 Rebound bed topography

The topography is the primary indicator of geological processes and geological type. In the sediment erosion, transportation and deposition process, the rock in the highland area is likely to be eroded. The eroded materials are then redistributed to form a sedimentary basin in the low topography area.

We remove the subsidence caused by ice thickness by releasing the current ice load. We estimate bed elevation before the ice expansion in Antarctica by calculating the rebound bed topography using BedMachine Antarctica¹². We assume an ice density of 917 kg/m³, sea water density of 1030 kg/m³, and mantle density of 3330 kg/m³ to remove the modern ice sheet load⁸². For areas below sea level, we iteratively calculate the load of water that replaces ice until the total load change is less than 2 meters.

1.3.1.2 Rebound bed topography variation

‘Bed topography variation’ is the irregular change of bed surface within a certain distance⁸³. Sediment is deposited in the low topographic areas during ice-free periods to form a sedimentary basin. The long term deposition process modifies the bed surface, which would cause the sedimentary basin to have an inherently smooth surface. In turn, the basement surface without sedimentary cover is rough. When the ice sheet interacts with its bed, the bed surface variation could be preserved or modified by the ice sheet during multiple glacial cycles¹⁵.

Here we calculate bed topography variation using the standard deviation of rebound bed topography in a 30 km window. Area with large errors (bed topography error larger than 500 m in BedMachine Antarctica¹²) is masked. To maximise the utility of multidimensional datasets, we replace the masked area with its global mean value (see session 1.4.1).

We note a potential bias of bed variation information due to radar data density variation and the inherent smooth data interpolation in BedMachine Antarctica¹². To illustrate this effect, we test the relationship of radar measurement density with bed variation for each geological type. We use the location where bed error is less than 30 m to represent the reliable data source in BedMachine data¹². We then calculate kernel density by a 16 km radius circular kernel. Based on Fig. S3, sedimentary basins and basement have different distributions in bed topography variation but with similar kernel density distribution. This distribution suggests that the discrimination of geology depends on its bed topography variation but is not associated with the data density variation. The low bed variation distributes through all data kernel densities for the sedimentary basin class. This supports a smooth nature for sedimentary basin.

The basement class has a larger bed variation in both high and low kernel density regions. Further, we calculate the Maximal Information Coefficient (MIC) of bed variation with kernel density (detail of MIC see 1.4.2). The MIC result (0.301) indicates a weak correlation between bed topography variation and kernel density. Overall, our training process is not highly biased by the heterogeneous data distribution.

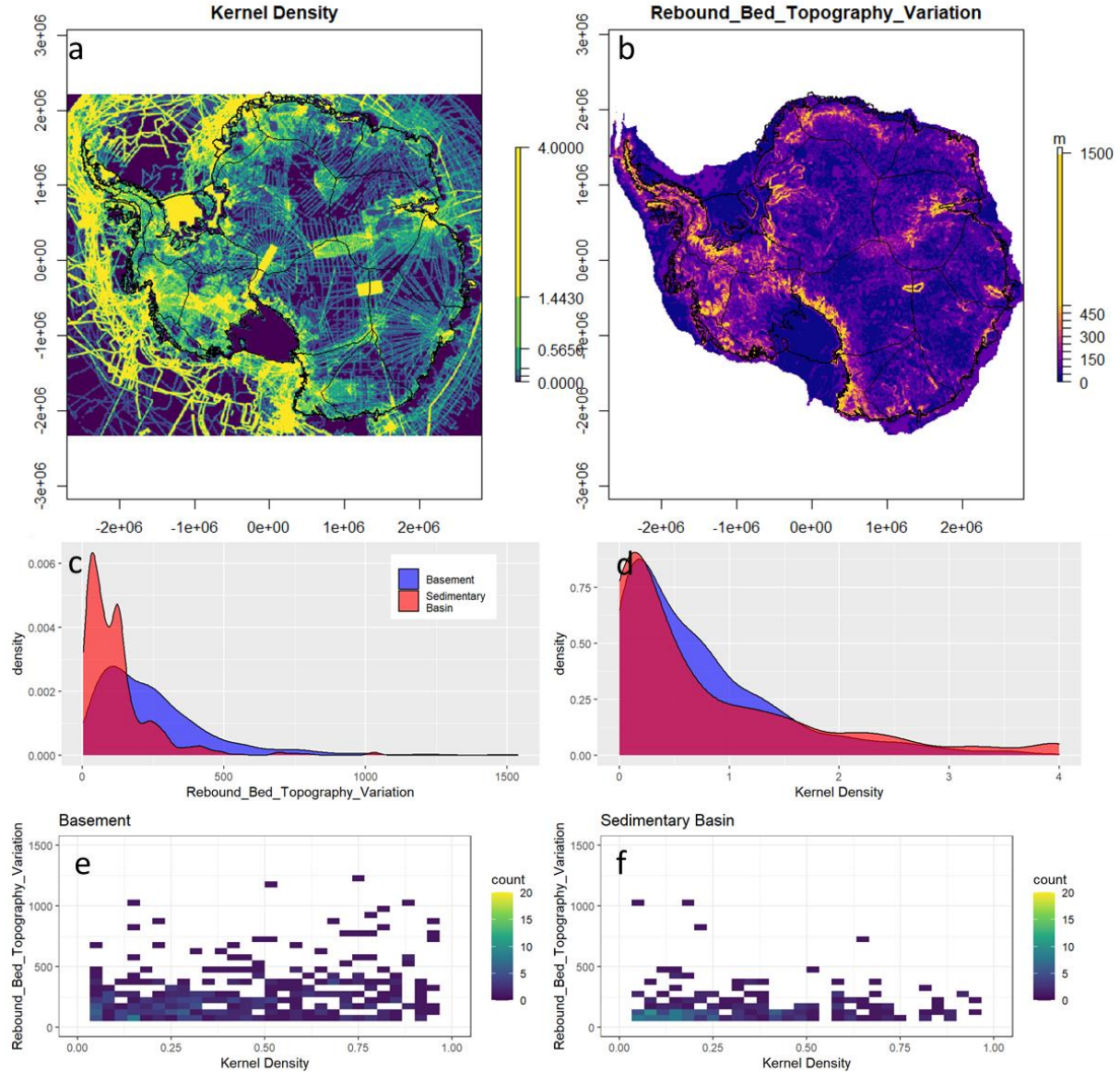


Fig S3. Topography variation versus kernel density of data measurement. The kernel density is calculated based on a 16 km radius circular window, which matches the area for topography variation estimation (30 km square window). The kernel density is shown in 5 zones based on histogram

equalization. The second row shows the density plot of topography variation and kernel density of data measurement for both sedimentary basin and basement classes. The third row shows cross plot between topography variation and kernel density for basement and sedimentary basin.

1.3.2 Gravity field

Gravity responds to the density variations in the subsurface. In a sedimentary basin, the low-density sediments fill in the topography low, making both free-air gravity and Bouguer gravity negative and smooth. Furthermore, isostatic gravity has removed the long-wavelength signal in the Bouguer gravity associated with the crust and mantle interface. Isostatic gravity anomaly could more directly reflect the upper crust density variation and subglacial geology⁷⁷.

1.3.2.1 Free-air gravity

The free-air gravity anomaly response is interpreted to reflect the bed topography signal. The low free-air gravity anomalies correspond to topographic basin and trench, and high free-air gravity anomalies correspond to mountain and dome¹³. The strong negative free-air gravity anomaly could be expected that low-density material fills and preserved in these low topographic areas⁸⁰.

We merge the continental-scale free-air gravity dataset AntGG¹³ with the latest gravity measurement in the South Pole⁸⁰, centre Marie Byrd Land⁸⁴, Ross Ice Shelf⁸⁵, and Recovery Lakes Region⁸⁶. We also use Global Marine Gravity V27⁸⁷ to fill the data gap without near surface measurement in offshore area. To merge these datasets, we upward continue these airborne free air gravity measurements to 5 km ellipsoid height. Then all these datasets are merged by blending to reference the GOCO06s⁸⁸ satellite gravity model.

1.3.2.2 Complete Bouguer Gravity and its residual

By removing the topography effect in free-air gravity, the Bouguer gravity reflects long-wavelength information caused by crustal thickness variation and short-wavelength variation caused by upper crust density variation.

We calculate the gravity effect of surface load using the reference density of 917 kg/m^3 , 1030 kg/m^3 , 1000 kg/m^3 and 2670 kg/m^3 for ice, ocean water, lake water and topography features, respectively. These features are regridded into geodetic coordinates at 0.05° resolution from BedMachine Antarctica¹². The 3D full terrain effect is then calculated using Tesseroids⁸⁹ within a 3° (333 km) radius around each grid point at 5 km ellipsoid height. The full terrain effect is subtracted to get the complete Bouguer gravity.

The continental-scale Bouguer gravity shows most of WA is positive, and EA is negative. This pattern is dominated by the long-wavelength signal, which is interpreted to be caused by thin crust in WA and thick crust in EA. This long-wavelength dominated signal hinders the utility of using Bouguer gravity amplitude to distinguish geology at the bed. To remove the effect of deep crustal structure signal, we calculate the residual gravity using a Gaussian high-pass filter of 500 and 1000 km wavelength.

1.3.2.3 Complete Bouguer Gravity Variation

The infilled sedimentary rock will flatten the short-wavelength information caused by the basement variation. The long-wavelength Moho signature is smooth. Hence, the variation of Bouguer gravity is assumed to represent the upper crust density change, indicating the subglacial geology variation.

Variable data sources and fight line spacing mean that the compilation of continent-scale datasets mixes different wavelength information. To match with bedrock topography variation analysis, we use a Gaussian high-pass filter in 60 km wavelength to calculate the residual gravity to reflect the near surface density variation. After that, we calculate the standard deviation of the filtered Bouguer gravity in a 30 km window size to compute the variation of the residual Bouguer gravity anomalies.

1.3.2.4 Isostatic residual gravity

The broad crust-mantle signals mask the near surface information and hinder the ability to use gravity to define upper crust information. Here, we assume a local Airy isostatic compensation. We also use the Moho depth (AN1)⁹⁰ driven by seismic tomography to remove the Moho signal in gravity data.

We convert ice, seawater, and lake water feature into equivalent topography, using density 917 kg/m^3 , 1030 kg/m^3 , and 1000 kg/m^3 , respectively. For the Airy isostatic model, we use the compensation depth of 30km with a density of 2800 kg/m^3 for the crust, with a 450 kg/m^3 density contrast⁹¹. After subtracting the isostatic response from Bouguer gravity anomaly, we use a 1000 km high pass filter to remove deep mantle signal.

1.3.2.5 Curvature from GOCE

The curvature of GOCE gravity gradient data provides a new perspective of the lithosphere domain and the tectonic boundary in the Antarctica continent⁹². The shape index and minimum curvature from topography and isostatic corrected GOCE gradient show several major tectonic structures in Antarctica. These tectonic settings reveal subglacial geology distribution.

1.3.3 Magnetic field

Sedimentary rocks usually contain little or no magnetisation. The magnetisation of basement is usually much higher than sedimentary rock. The short-wavelength signal produced by basement is masked when it's overlain by sedimentary features to show a relatively smooth magnetic signal. Moreover, high-frequency and high-intensity signals are rare in a sedimentary basin, except where volcanoes are present.

1.3.3.1 TMI and residual

The total magnetic intensity (TMI) of the PolarGAP⁸⁰, ROSETTA-Ice⁸⁵ and IceGRAV⁸⁶ surveys are smoothly stitched to the ADMAP-2 dataset using a fast Fourier Transform suturing method. The new magnetic compilation is reduced to the magnetic pole using the differential reduction to pole (DRTP) method⁹³. We filter the wavelengths $> 1000 \text{ km}$ to remove the effect of deep magnetic sources.

1.3.3.2 TA

Total Amplitude (TA) of magnetic vector is the amplitude of magnetic vector (three components) data, which has been used for magnetic data interpretation in large area⁹⁴. It is weakly dependent on the

magnetization direction, thus less affected by the remanent magnetizations. We transform the TMI field to TA by assuming geomagnetic field direction as the magnetization direction⁹⁵.

1.3.3.3 *TMI variation*

We calculate the magnetic variation using the standard deviation of the DRTP-TMI response in 30 km window size after high pass filtering 60 km wavelength. We also use the Analytic Signal Amplitude of DRTP-TMI to highlight the short-wavelength information. The variation coincides with continental margins with exposed basement due to glacial erosion¹⁵. Extreme high short-wavelength variation distributed from Ross Ice Shelf to the Marie Byrd Land is interpreted to be volcanic rock. The smooth magnetic signal in the inner continent is associated with thick ice coverage. The Transantarctic Mountains show the non-magnetic character within meta-sedimentary and meta-volcanic outcrops area. In West Antarctica Rift System, the rough magnetic anomaly variation is interrupted by a less magnetised feature, which corresponds to the inferred sediment fill by the Werner filter method⁷⁵. However, due to the strong magnetised volcanic rocks, the overall area shows a rough magnetic response.

1.3.3.4 *Pseudo-gravity and its residual*

Pseudo-gravity transform enhances the long-wavelength information of the magnetic source, which can illustrate regional deeper magnetic source variation. Following the work of Salem, et al.⁹⁶, we integrate the DRTP-TMI field and normalise it with the ambient magnetic field. We then calculate the residual of pseudo-gravity by a Gaussian high-pass filter of 1000 km to remove the magnetic signal due to very deep crustal architectures.

The residual pseudo-gravity shows several strong negative anomalies in the thick metasedimentary basin proximal to the Ellsworth–Whitmore Mountains, the Beacon supergroup in the Transantarctic Mountains, and the metasedimentary rocks in Victoria Land.

1.3.4 Cryosphere and Solid-Earth Structure

The relationship between earth structure and ice sheet properties to the geological type is complicated and remains unclear. Here we use crustal thickness⁹⁰, heat flux⁹⁷, ice flow speed⁵⁴ and basal friction⁹⁸ as input features. We aim to test the relationship between these properties with the subglacial geological condition and understand the potential interactions between the cryosphere and solid-earth.

1.4 Methods

1.4.1 Input feature processing

While geophysical data collection in Antarctica is ongoing, there are still large data gaps in the current continental-scale data compilation (Fig. S4). Where possible we have endeavoured to fill data gaps with the latest publicly available airborne geophysical measurement. To maximise the utility of the multidimensional datasets, we impute the evidence feature to generate a complete multi-dimension dataset. We fill the data gaps using the global mean value of each dataset.

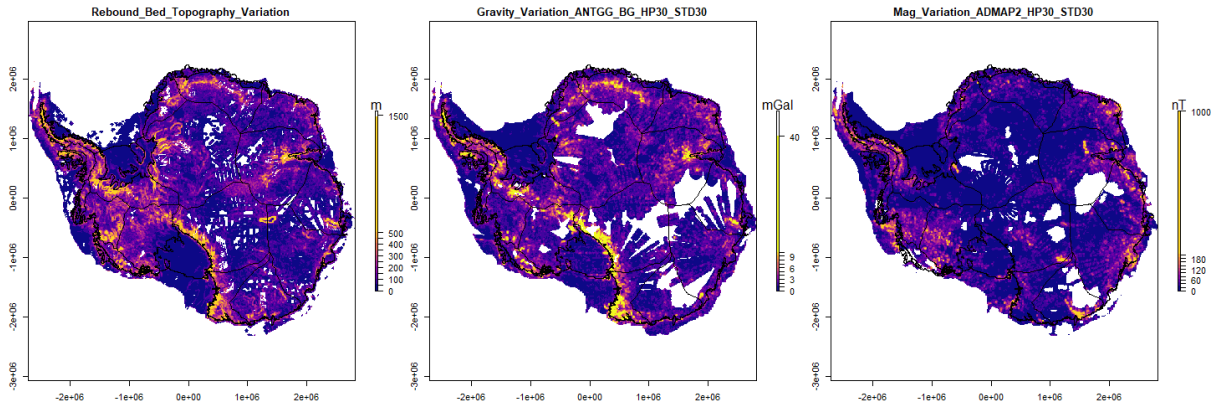


Fig. S4 Major data gaps in the current continental-scale data compilation. The bed topography variation data is masked where BedMachine Antarctica¹² error is larger than 500 m. The gravity and magnetic data gaps reflect areas without airborne measurements. For Free-Air gravity data, this data gap is filled by GOCO06s⁸⁸ satellite gravity model. For gravity variation analysis, this data gap is filled by its global mean value as short-wavelength information is poorly constrained in satellite gravity data.

1.4.2 Input feature reduction

Highly correlated input features indicate duplicate and unnecessary information. The inclusion of duplicate information lowers model performance and model interpretability. We use a two-step approach for input feature selection⁹⁹. We estimate the importance of input features using the Boruta method¹⁰⁰. We then use the Maximal Information Coefficient (MIC) to measure the independence of input features. According to the RF OOB (out-of-bag) error metrics, the highly correlated and unimportant input features are removed.

In Boruta algorithm, copying and randomising input features are added to the model domain to form shadow attributes¹⁰⁰. It trains a RF model and computes the Z scores. The Maximum Z score among Shadow Attributes (MZSA) is then used to measure the importance of features. The original input feature is important if its feature importance score is significantly higher than MZSA, while it's unimportant with feature importance score is significantly lower than MZSA. The algorithm stops when all features' importance is calculated, or reaches the maximum RF runs limitation.

The MIC estimates the highest normalised mutual information of two features estimated by different bins¹⁰¹. Mutual information is based on whether the relationship between two features could be captured by scatterplots from different subsets of the data. MIC is zero for two statistically independent features and close to one for highly correlated features. We use the R package Minerva to calculate the MIC for all features¹⁰².

In the following step, we test the influence of the model performance with the correlation of input features. We test using evidence with MIC ranging from 0.1 to 1 and assess using the model OOB errors in RF. In each test, we remove the correlated input features with lower importance and keep the feature with higher importance based on the Boruta input feature importance score.

1.4.3 Training Point Sampling

The performance of the supervised machine learning method depends greatly on the training point during training process. For the lithology and geology mapping problem, sparse training data with a spatially balanced class sample is preferred, as it limits the bias associated with prior knowledge and reduces the risk of overfitting^{11,52}. This is an important consideration in this study, as we generate training information from different sources with variable uncertainties. The spatially balanced and sparse training points could maintain the prior information and reduce the chance of overfitting in the misclassified or complex geology type.

Training points are located in a reference grid (fishnet) with a 100 km cell size to maintain spatially even distribution. For each cell in the fishnet, we randomly sample one point in each type of geology within the overlapping area of the training polygon and the fishnet cell. By doing this, we obtain spatially even distributed training information with 612 points for sedimentary basin and 608 points for basement. We further reduce sedimentary basin training points to 608 points by a random subsampling. This generates a balance in the subclass and spatially even distributed training set with near 3% of total training area. The sampling process is illustrated in Fig. S5.

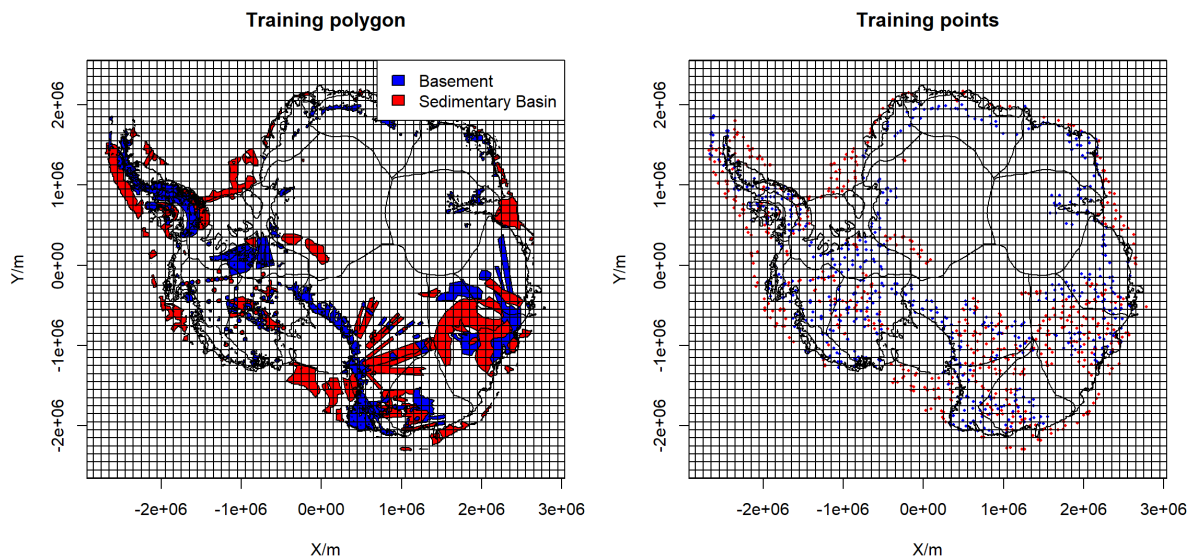


Fig. S5 Illustration of the sampling process using a reference fishnet with a 100 km cell size. At left: Training polygon overlie with reference fishnet. At right: Red dots indicate sampled sedimentary

basin; blue dots indicate sampled basement. We sample a maximum of 1 point of sedimentary basin and basement in each fishnet cell.

1.4.4 RF Model training

RF has several hyper-parameters to control the training process, including the number of trees (ntree), the number of input features to use at any given split (mtry). These hyper-parameters might have a large influence on model accuracy. We use a grid search method to test the influence of these two hyper-parameters to the RF training accuracy. The RF training accuracy is estimated by 10-fold cross-validation with three times repetition.

After selecting the hyper-parameter, we use a balanced number of sedimentary basin and basement training points for model training (608 points in each class). We repeat the training point sampling process using the reference fishnet grid 10 times to maintain a stable and unbiased result. We generate a sub-RF model based on the sampled training points each time. Each sub-RF model result indicates a representation of subglacial geology distribution. We use the mean of 10 sub-RF predictions to determine the final likelihood for subglacial sedimentary basin distribution.

RF use the mean decrease in accuracy or node purity to estimate the relative importance of input features. The node purity might be biased when input features vary in their dynamic range¹⁰³. Here we use the mean decrease in accuracy to measure the importance of input features. The mean decrease in accuracy measures the model performance with one input feature is assigned randomly, and the rest of the input features unchanged. The input feature is more important when model accuracy decreases most in its absence.

1.4.5 Accuracy measurement

Cross-validation (CV) is widely used to evaluate the model performance without independent validation data, such as in this case where we lack ground truth information. However, CV tends to overestimate the model performance due to geophysical data representing the volume response of rock properties

with spatial correlation¹⁰⁴. To overcome this problem, we use a 10 fold block CV to evaluate the model performance¹⁰⁴. In here, we divide the whole model domain into 10 rows with 10 columns of equal-sized blocks. Area without training data is omitted from this process. Blocks are then randomly assigned to a ‘fold’ until each fold has a similar amount of training points (Fig. S6). Each fold has roughly 60 sedimentary basin and basement training points.

In the 10 fold cross-validation process, 9 folds are used to train a RF model, with the remaining 1 fold being used to validate the model result. The whole process loop through all folds to ensure each fold is used for validation. The CV result is summarised in the confusion matrix (Table. S2), which shows the distribution of consistent and inconsistent classification distribution. The model's overall accuracy is indicated by the percentage of the consistent result of model prediction with the validation set during the block CV process.

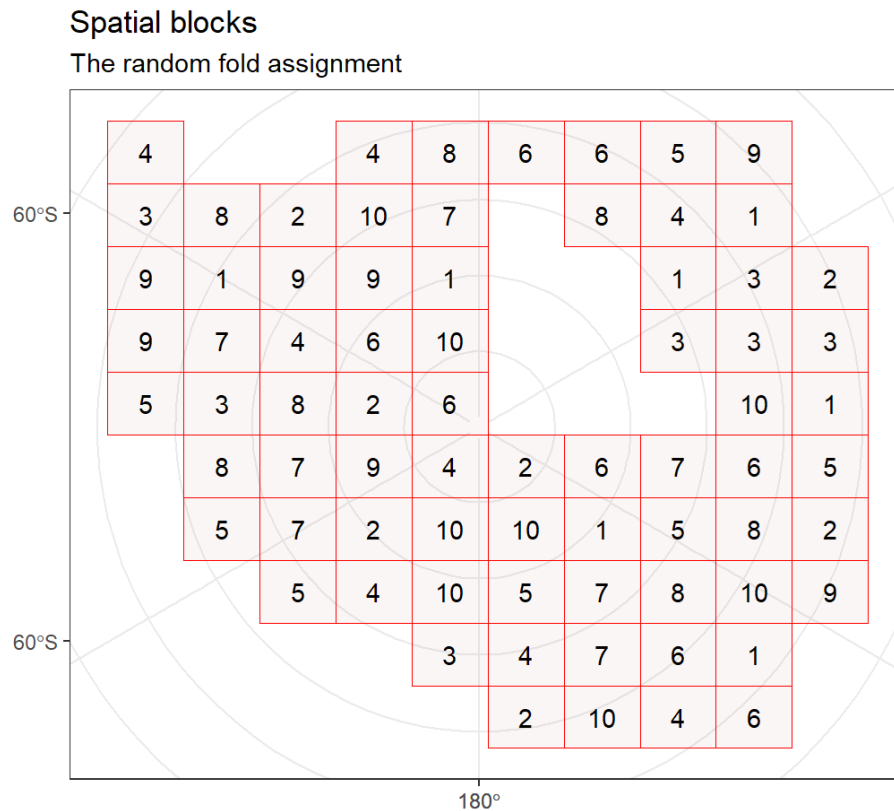


Fig. S6 Illustration of the folds in block CV process. The area with training data is divided into spatial

blocks. Then blocks are randomly assigned into 10 folds (numbers in the box) until each fold has a similar number of training points (roughly 60 SSB and basement points).

1.5 Result

1.5.1 Input feature selection

24 evidence features were all deemed important in the Boruta analysis, with max 500 times importance source runs and a confidence level of 0.5 (Fig. S7).

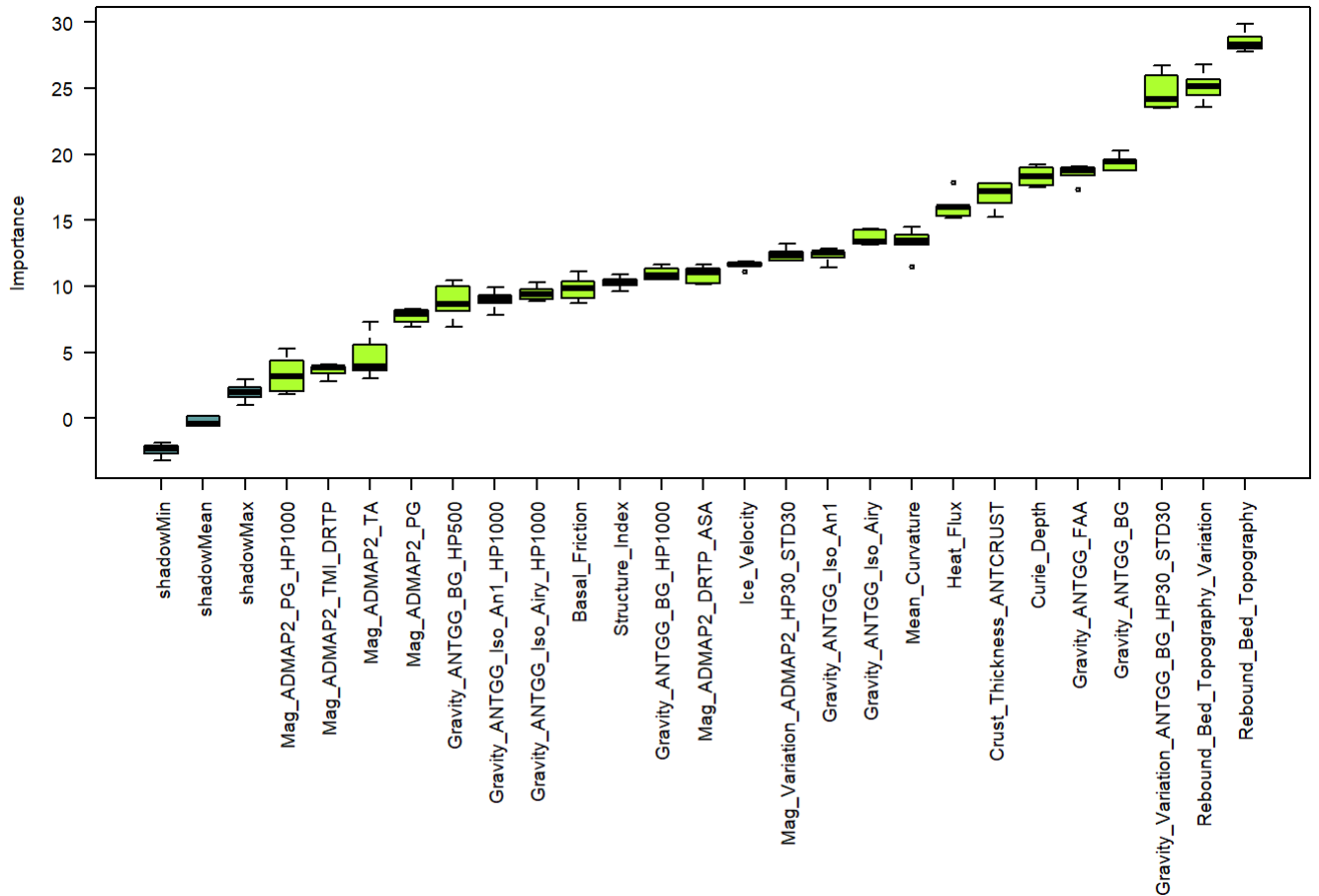


Fig. S7 Model importance generated by Boruta variable selection. All input features are important as they are higher than maximum shadow variables.

Based on a plot of the RF OOB error estimates over the MIC, a value of 0.71 was selected (Fig. S8).

This selection ensured higher model performance while at the same time minimising the number of

predictor variables by removing highly correlated and unimportant input features. The final 20 input features were used for the RF model training (Fig. S9). These features include rebound bed topography, rebound bed topography variation, gravity variation, Bouguer gravity, Free-Air gravity, Curie depth, crust thickness, Airy isostatic gravity, mean curvature, magnetic variation, ice velocity, Bouguer gravity residual (high pass filter 1000 km), analytic signal amplitude, basal friction, Airy isostatic gravity residual (high pass filter 1000 km), An1 isostatic gravity residual (high pass filter 1000 km), Pseudo-gravity, total amplitude of magnetic vector, total magnetic intensity after reduction to pole, and Pseudo-gravity residual (high pass filter 1000 km).

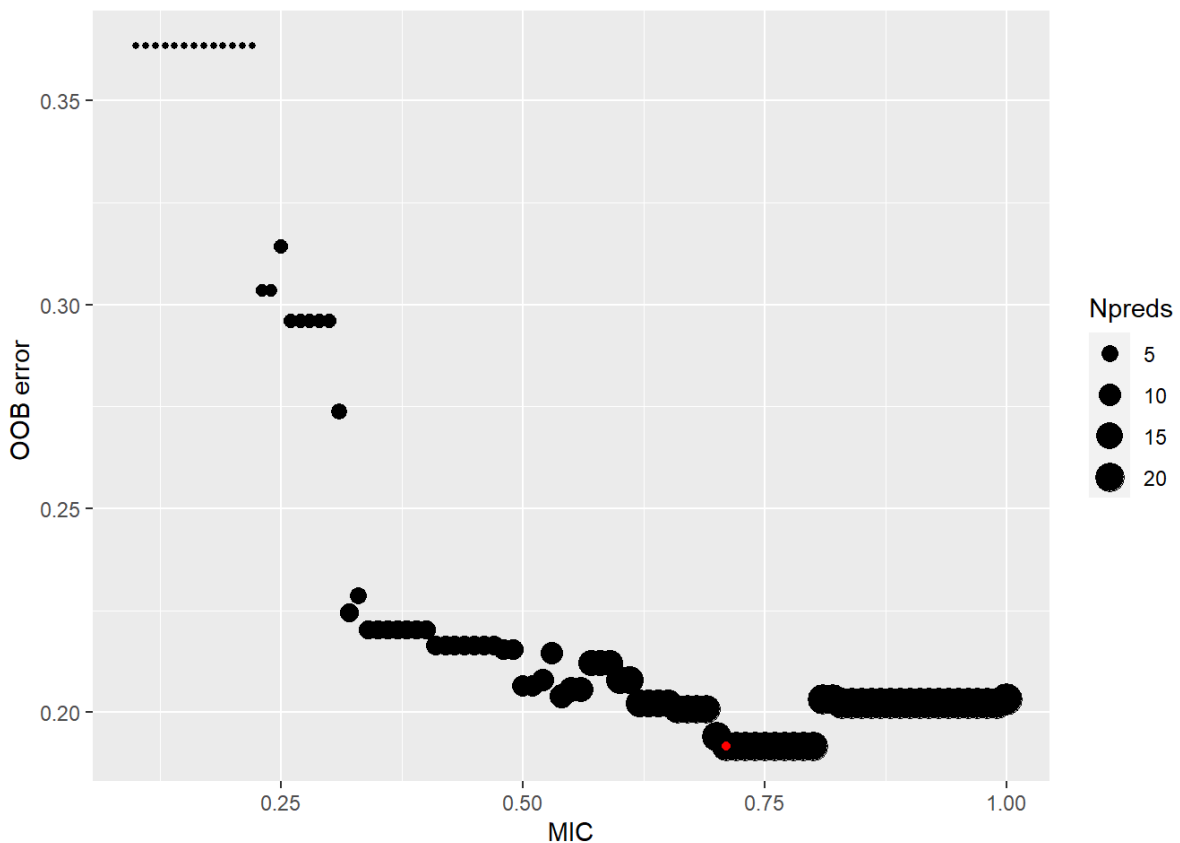


Fig. S8 Influence of MIC on the out-of-bag error of RF model. The red dot ($\text{MIC}=0.71$) shows the cut off value of MIC with low OOB error and the number of input features.

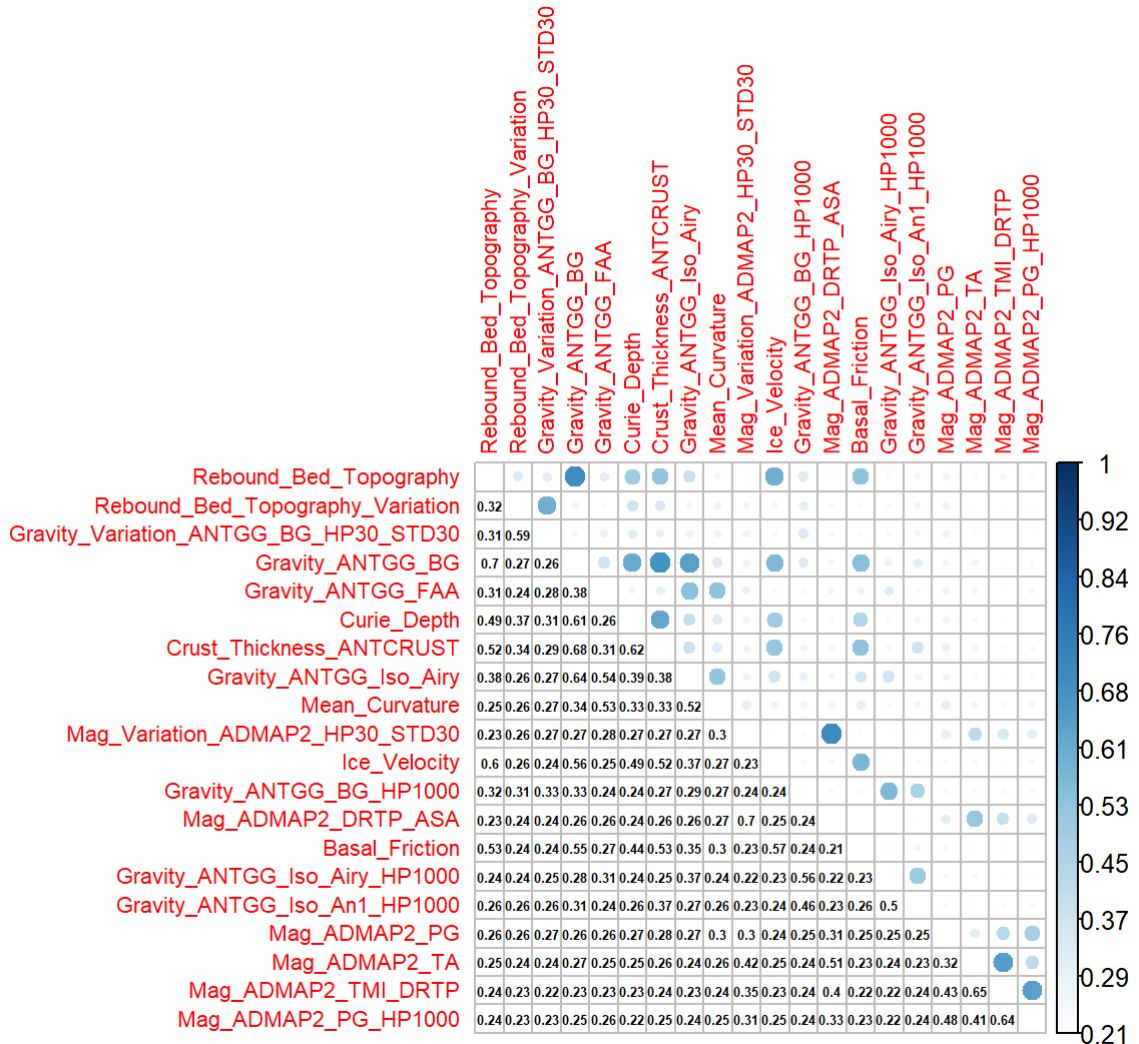


Fig. S9 Correlation plot (MIC) for all selected input features. The maximum correlated features are Bouguer gravity and rebound bed topography.

1.5.2 Model tuning

We use a grid search method to check the RF OOB error with the influence of mtry and ntrees. The mtry change from 2 to 20 with 2 intervals. The ntrees change from 400 to 1000 with 100 intervals.

Based on the CV accuracy, the model performance is stable by changing hyperparameters (Fig. S10). The maximum difference is less than 0.02. We find the maximum CV accuracy is achieved with mtry = 2, and ntrees = 500. We then use these hyperparameters to build RF model.

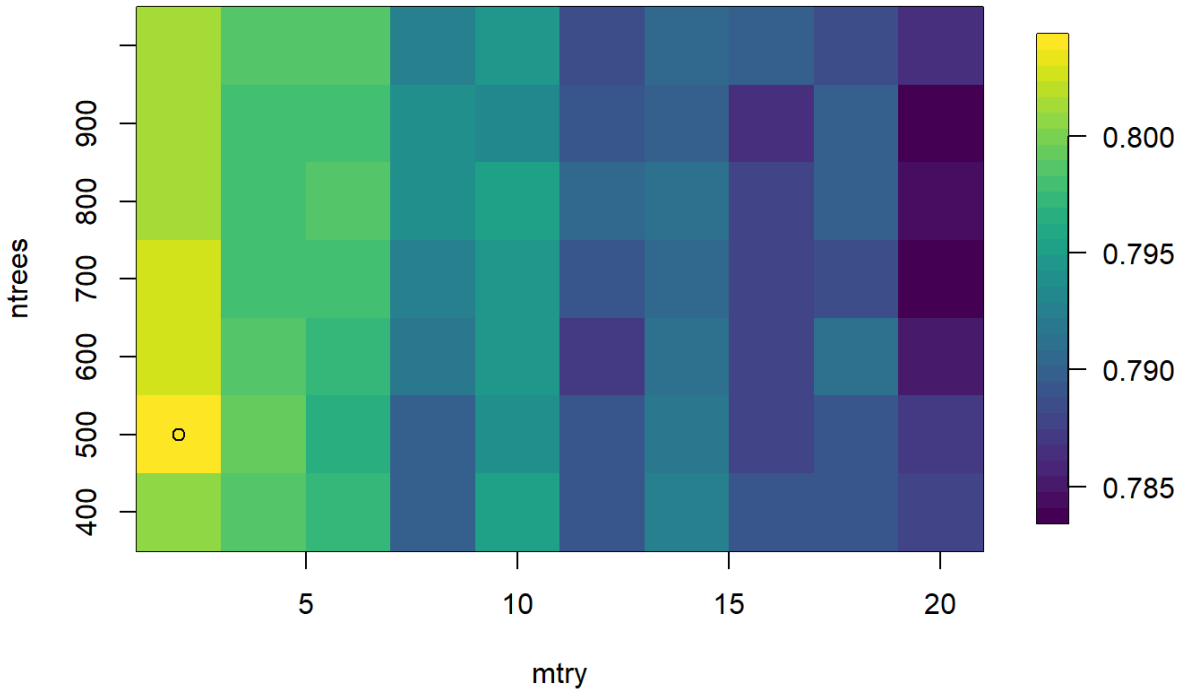


Fig. S10 CV accuracy with various mtry and ntrees for RF model tuning. The maximum accuracy is achieved with mtry=2 and ntrees=500.

1.5.3 Model accuracy and uncertainties

In here, we would like to communicate the model accuracy and uncertainties in three ways. At first, we compare the RF prediction with the prior training information. This indicates the discrepancy between all prior information with the RF model result. Then, we check the spatial distribution of the consistent and inconsistent prediction during the block cross-validation process. This information could reflect how RF model performs in an area without training information. In the end, we show the internal variation of 10 sub-RF model outputs, which indicates the uncertainty of the RF model during the training point subsampling and training process.

For a cell to cell comparison with all initial training information (Fig. S11), 2453 cells of basement training information (6.7% of the total) are inconsistently classified as sedimentary basin, 1068 cells of

sedimentary basin training information (2.9 %) are inconsistently classified as basement. The remaining 33098 cells (90.4%) are consistent with RF output.

Each sub_RF model uses different training points by resampling from the training information. We show the 10 fold block CV result for each sub_RF model (Table. S2). We see that each sub_RF model has similar model accuracy. Combining all these results, the model has an overall model accuracy of 77.9%, with 95% confidence limits of 77.1% and 78.6% (Table. S2). We combine all training points used in the 10 sub_RF models and then use 10 fold block CV to show the total model accuracy. This result shows the model's total accuracy is 79%, with 95% confidence limits of 78.3% and 79.7% (Table. S3).

Although the model performance during block CV does not directly translate to the unknown area without training information, it indicates the utility and weakness of the RF model when applied to areas without training information. The incorrectly classified training points during block cross-validation are shown in Fig. S12. We note that the majority of training points inconsistent with the prediction are located at the boundaries between sedimentary basin and basement. Most other training points are relatively consistent during the CV process.

The standard deviation of 10 sub-RF models represents the variation of sedimentary basin likelihood (Fig. S13). In general, we find a large likelihood variation at the geological boundaries. The highest likelihood variation is located at the Antarctica Peninsula.

Fig. S13d shows the frequency when a location is predicted as a sedimentary basin (likelihood > 0.5) for all sub_RF models. Although the sedimentary basin likelihood value varies in each sub_RF model during the training point sampling process, the classified sedimentary basin in each model is consistent. This pattern suggests the broader sedimentary distribution is consistent but with some small variation at the margin. The overall classification result is robust during the subsampling and training process.

We further show the correlation between the consistent and inconsistent training points with the STD of all sub_RF likelihood (Fig. S14). For the mean RF prediction result compared with the initial training information (all information in the training polygon), the consistent prediction is located in the low likelihood variation area, while the inconsistent prediction has a relatively higher likelihood variation (Fig. S14d). This effect is further amplified during the block CV process. We see a large difference in the distribution of consistent and inconsistent predictions. The median of a consistent classification has a STD of 0.05, while the inconsistent classification has a STD of 0.129 (Fig. S13b).

These incorrectly classified points during block CV could be attributed to the inherent complex geology in its setting and/or the geology boundary and/or potentially incorrect training information. In Antarctica Peninsula, the sedimentary rock outcrop is misclassified as basement, as it is extensively intruded by volcanic rocks¹⁰⁵. The misclassified sedimentary basin in West Antarctic Rift System is associated with the positive gravity response and is surrounded by volcanic rock, supporting a complex signal in its geophysical response⁷⁵. In Wilkes Land, the narrow Knox subglacial basin and strong reverse magnetic signature in Law Dome indicate the unique geological setting. The Sabrina Subglacial Basin shows several misclassifications in its internal area. The overlying ice sheet has been proposed to retreat and advance several times^{15,106}. Past glacier activities are likely to thin the sedimentary basin and change its geophysical response in this area.

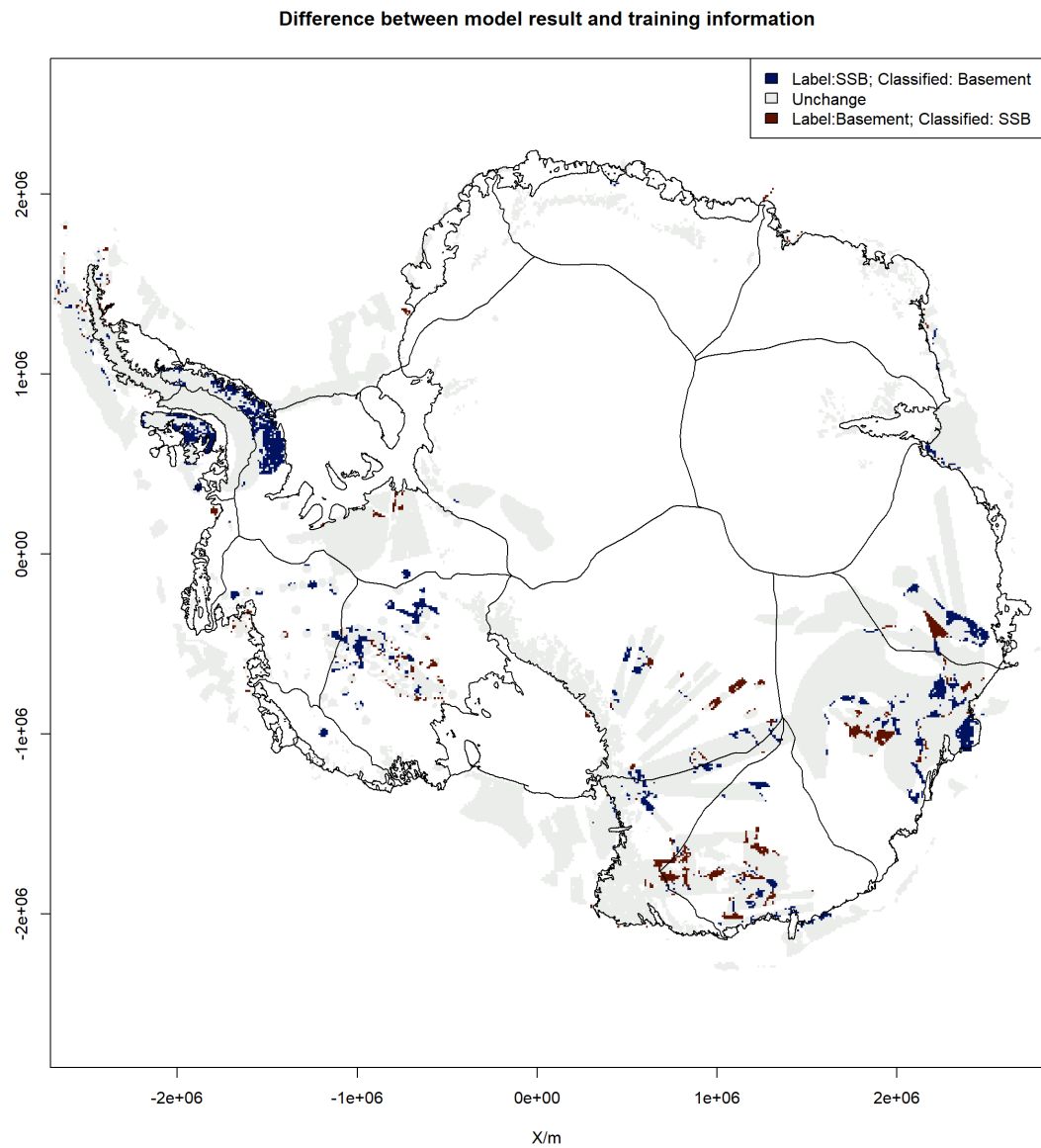


Fig. S11 Comparison of RF result with the initial training information as consistent (white) and inconsistent (red and blue). Red represents locations labelled as basement but classified as subglacial sedimentary basin (SSB). Blue represents locations labelled as SSB but classified as basement.

Inconsistent classification during block CV

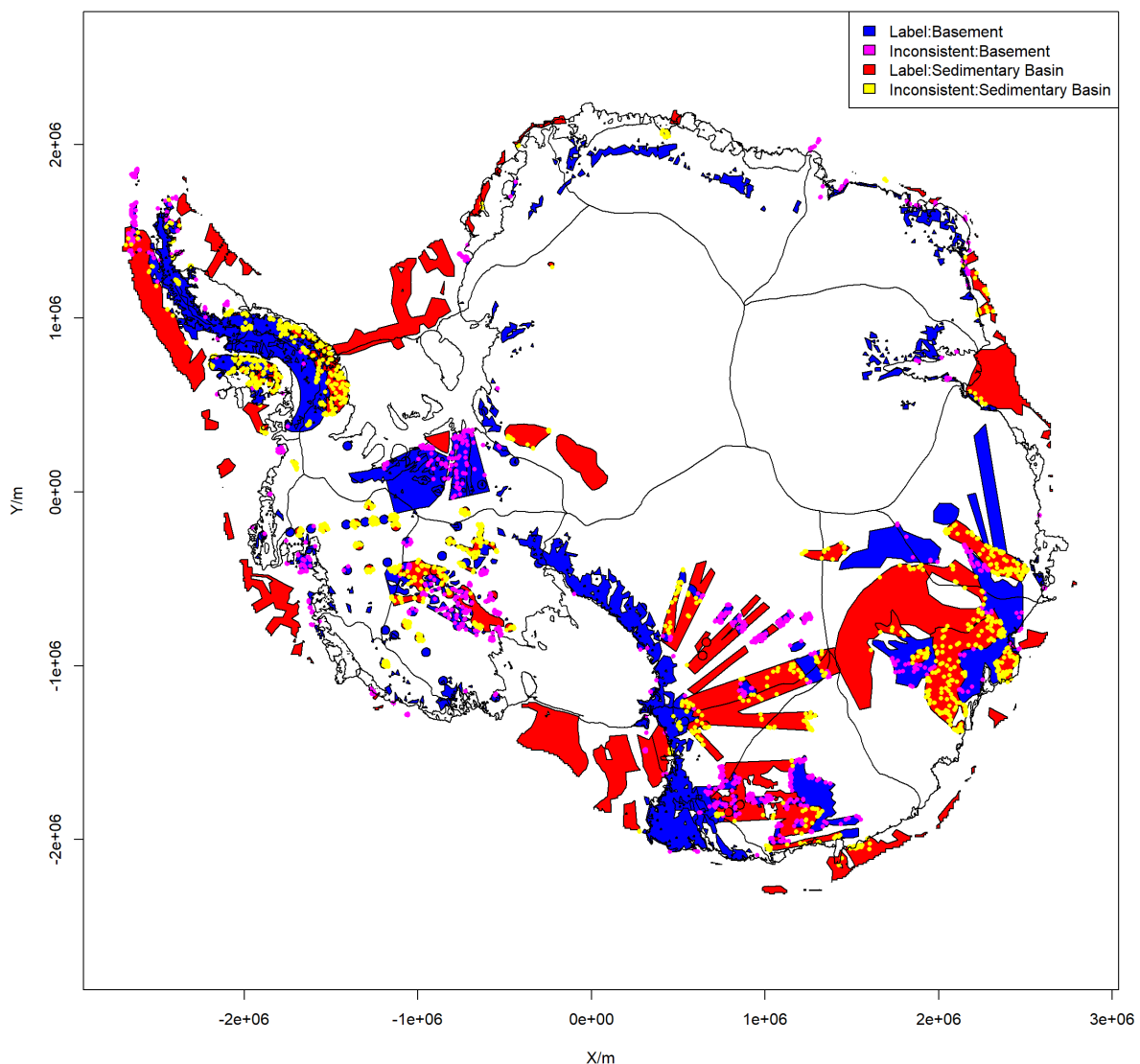


Fig. S12 Inconsistent classification result during 10 fold block CV. Yellow dot shows labelled sedimentary basin is classified as basement during CV process; magenta shows labelled basement is classified as sedimentary basin.

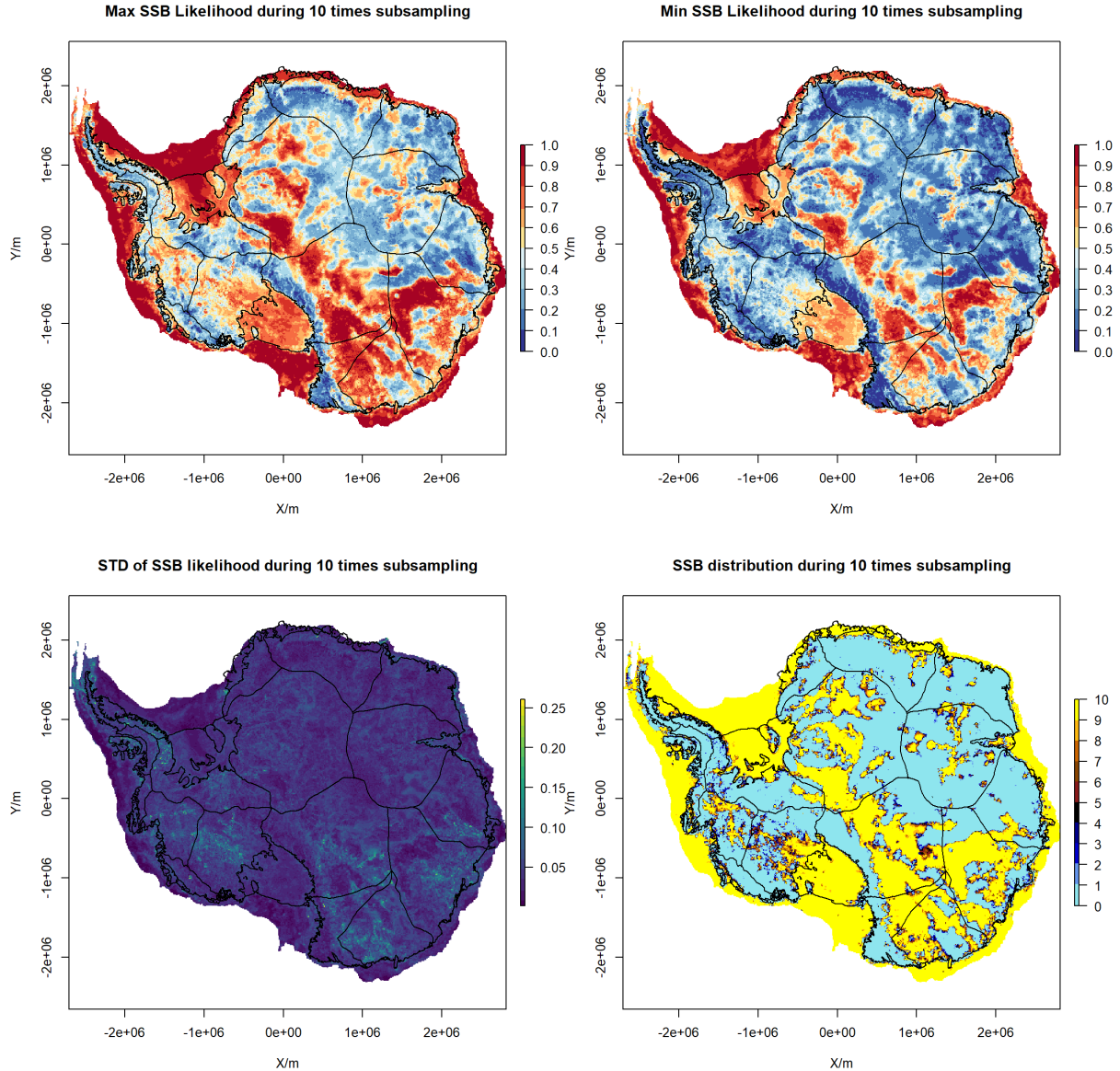


Fig. S13 Maximum, Minimum, and STD of SSB likelihood and classified sedimentary basin for all sub_RF models. The maximum and minimum likelihood show the confidence in the classification using different training information. The likelihood variation is high in geological boundaries, and may reflect the complexity of geological conditions. Assume likelihood 0.5 as the boundary of SSB and basement. The SSB distribution score shows the total time when a certain location is classified as SSB. In total, 82% of data areas return consistent results (class 0 or 10) for all 10 sub_RF runs.

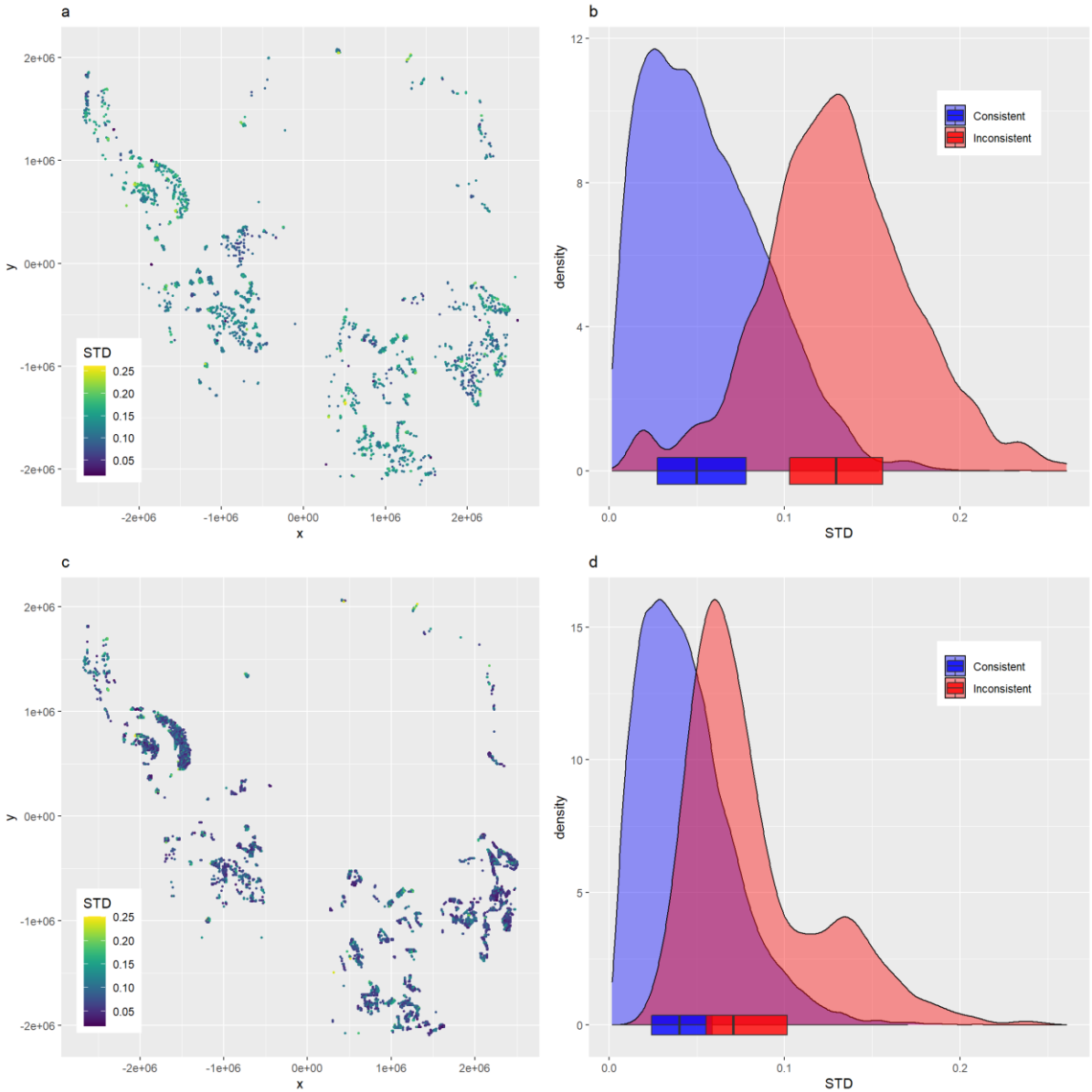


Fig. S14. The correlation of consistent and inconsistent classification with the STD of all sub_RF models. **a**, the STD of SSB likelihood of inconsistent training points during the 10-fold block CV. **b**, density plot of the STD of SSB likelihood of consistent and inconsistent training points during 10-fold block CV. **c**, the STD of SSB likelihood of inconsistent initial training information. **d**, density plot of the STD of SSB likelihood of consistent and inconsistent initial training information.

1.5.4 Input feature importance

The RF input feature importance for all sub-RF 10 models is shown in Fig. S15. The most important information is related to bed topography and Bouguer gravity. Then the following input features are related to the variation of bed topography and gravity. Free-Air gravity, Curie depth, crust thickness,

ice velocity, mean curvature, Airy isostatic gravity and basal friction are ranked with relative higher importance, reflecting the tectonic setting and basal conditions for ice flow.

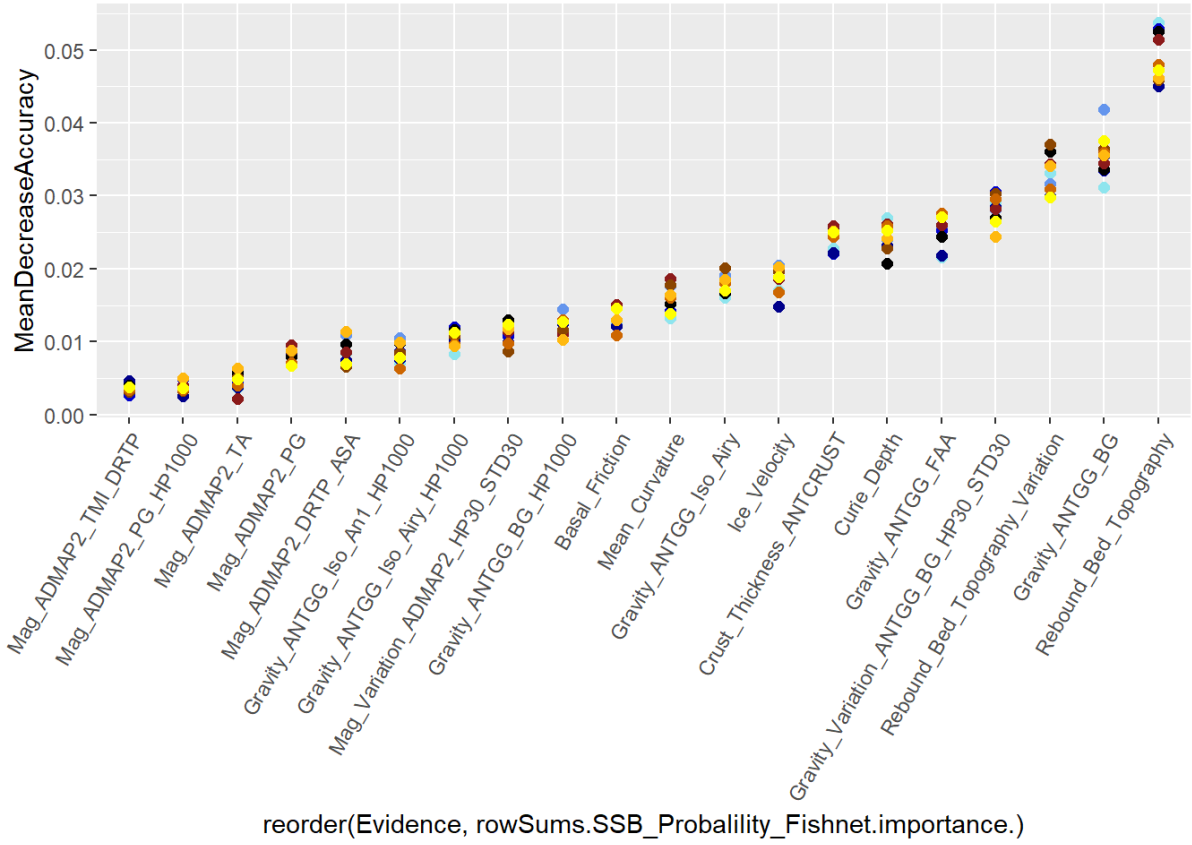


Fig. S15 Mean decrease accuracy of input features ranked by RF. The colored dot shows the mean decrease accuracy variation in all 10 sub-RF models. We rank the evidence importance based on the mean value of mean decrease accuracy of all 10 sub-RF models.

1.5.5 Sensitivity test

We further test the model change with reference sampling fishnet by shifting the whole fishnet in the top and right half-cell size (50 km). We repeat the same training point resampling and model classification and test the model performance after changing the reference training point.

The overall RF classification performance difference is minimal (Fig. S16). We see the majority difference in sedimentary basin likelihood is less than 0.1, with the largest change located in the interior of West Antarctic Rift System. We note that the volcano sediment nature¹⁰⁷ supports an inherent uncertainty in this region. The other large change is located in the inner Sabrina Subglacial Basin. The

natural setting of this area is a mixed sedimentary basin with basement zone due to prior glacial retreat and advance¹⁵. The rest of variation is shown by the linear feature in the classification result, indicating the geological boundaries.

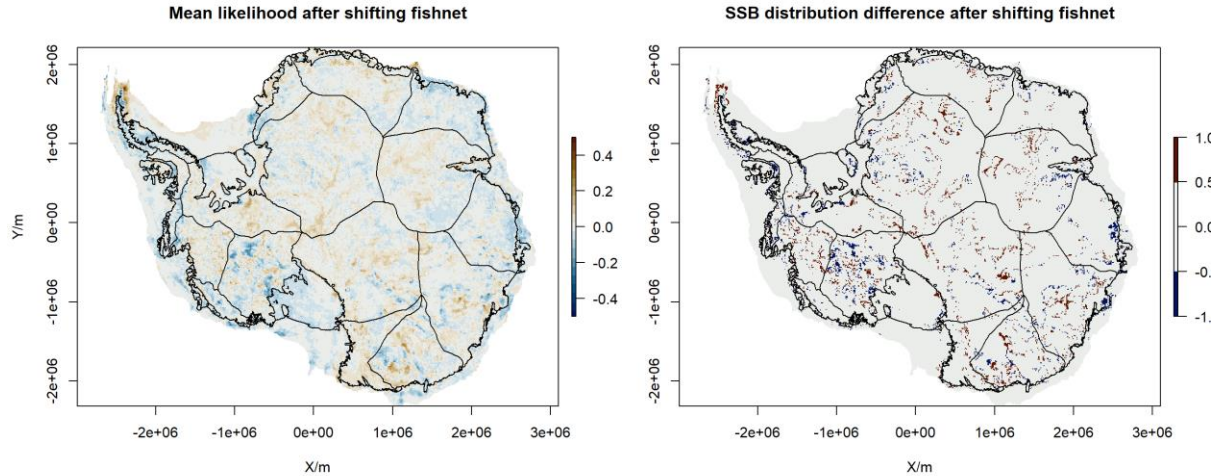


Fig. S16 The likelihood variation and classification difference of RF model using different fishnet. The positive likelihood variation indicates a reduction of sedimentary basin likelihood using a shift fishnet. The negative likelihood variation indicates an increase of sedimentary basin likelihood using a shift fishnet. The blue area means the geology is classified as basement by original fishnet, but as sedimentary basin with shifted fishnet. Red area means the geology is classified as sedimentary basin by original fishnet, but as the basement with shifted fishnet.

1.6 Model limitation and robustness

This study utilises a predefined subglacial geology map to reclassify subglacial bedrock types beneath Antarctic ice-sheet. The result has defined sedimentary basins in Antarctica with an accuracy of 78%. However, this approach has suffered some drawbacks due to missing knowledge (inaccessible of Antarctic ice-sheet bed) and the limitation of the current generation of Antarctica datasets.

1.6.1 Uncertainty in training point calibration

The training points are primarily generated by the integration of interpreted subglacial geology. The inaccessible Antarctic ice-sheet makes the training point selection difficult and uncertain. A typical

example is the misclassified information in the northern Wilkes Subglacial Basin, where basement training points are classified as sedimentary basin. The interpretation of aeromagnetic data indicates thick metasediment preservation in the eastern Wilkes Subglacial Basin. It also suggests modern sedimentary basins are mainly preserved in the magnetic low area, with the rest positive anomaly region showing basement structure⁷⁸. Inversion of gravity data suggests a broader distribution of sedimentary basin with variable sedimentary basin thickness. This misclassified area shows the thickness of 100-300 m of sedimentary basin by gravity inversion. These thin sedimentary features are close to the uncertainty range of the current continental-scale gravity dataset (10 km cell size). This uncertain information does have a contribution to the model uncertainty. However, this uncertainty is unavoidable with most subglacial geological interpretations performed using airborne geophysics data.

1.6.2 Uncertainty in input features

The model importance shows the topography, Bouguer gravity and topography variation ranked top-3 among all evidence features to classify sedimentary basin and basement. The inherent smoothing by data interpolation in continental-scale geophysical datasets could produce a smooth texture that artificially inflates sedimentary basin distribution and underestimates basement distribution. It's especially in central East Antarctica, where large line spacing geophysical measurements smooth the geology signal. As noted in newly collected airborne gravity data in Dronning Maud Land, the West Ragnhild Trough anomaly is much sharper and deeper compared with the ANTGG dataset¹⁰⁸. However, the latest bedrock topography model (BedMachine V2), and updated AntGG gravity model have greatly improved the data coverage and reduced uncertainties in the continental-scale dataset. Especially in the fast-flow region, the mass conservation approach has resolved the large-scale geometry of bed topography.

1.6.3 Model robustness

Although the model result is limited by the uncertainty in both training point and evidence features, our result is still robust, especially in the upper catchments in Antarctica. These areas have a consistent RF model prediction with a relative low STD. Meanwhile, since the 1990s, airborne geophysical

measurement has started to focus on the onset of ice streams²². The overall data quality over the fast-changing ice stream is high compared with the interior continental region. These rich data measurements improve the confidence of bed classification in these regions. Meanwhile, we loosely constrain the subglacial geology during the classification by subsampling the interpreted geology using a reference fishnet. The 10 times subsampling and training process gives a good balance of model variability and accuracy. The result shows a large area with a consistent RF classification result. We also test the influence of reference fishnet on the model performance by shifting its location. The model results with different fishnets are mainly consistent. The major difference is located at several geology boundaries.

Overall, we implement a robust workflow for the sedimentary basin distribution mapping. The model could be easily updated when new knowledge (training points) and new measurements (updated input features) become available.

2 Hydro-mechanical model

2.1 Method

2.1.1 Geomechanical Modelling

The lithosphere deformation u_x and u_z due to ice sheet weight is solved by a 2-D plane strain elasticity equation:

$$\begin{aligned}\frac{\partial}{\partial x} \left[C_{11} \frac{\partial u_x}{\partial x} + C_{12} \frac{\partial u_z}{\partial z} \right] + \frac{\partial}{\partial z} \left[C_{33} \left(\frac{\partial u_x}{\partial x} + \frac{\partial u_z}{\partial z} \right) \right] &= 0 \\ \frac{\partial}{\partial x} \left[C_{33} \left(\frac{\partial u_x}{\partial x} + \frac{\partial u_z}{\partial z} \right) \right] + \frac{\partial}{\partial z} \left[C_{11} \frac{\partial u_x}{\partial x} + C_{12} \frac{\partial u_z}{\partial z} \right] &= 0\end{aligned}$$

where $C_{i,j}$ are the material coefficients, including Young's modulus E and Poisson's ratio ν . It is defined by:

$$C = \begin{bmatrix} \frac{E(1-\nu)}{(1-2\nu)(1+\nu)} & \frac{E\nu}{(1-2\nu)(1+\nu)} & 0 \\ \frac{E\nu}{(1-2\nu)(1+\nu)} & \frac{E(1-\nu)}{(1-2\nu)(1+\nu)} & 0 \\ 0 & 0 & \frac{E}{2(1+\nu)} \end{bmatrix}$$

After solving the lithosphere deformation, the horizontal σ_{xx} , vertical σ_{zz} , out of plane normal stress σ_{yy} , and total normal stress σ_{kk} can be calculated as follows:

$$\left\{ \begin{array}{l} \sigma_{xx} = \sum_{i=1}^9 \frac{Ev}{(1-2\nu)(1+\nu)} \left[\frac{1-\nu}{v} \frac{\partial u_{x,i}}{\partial x} + \frac{\partial u_{z,i}}{\partial z} \right] \\ \sigma_{zz} = \sum_{i=1}^9 \frac{Ev}{(1-2\nu)(1+\nu)} \left[\frac{\partial u_{x,i}}{\partial x} + \frac{1-\nu}{v} \frac{\partial u_{z,i}}{\partial z} \right] \\ \sigma_{yy} = \sum_{i=1}^9 \frac{Ev}{(1-2\nu)(1+\nu)} \left[\frac{\partial u_{x,i}}{\partial x} + \frac{\partial u_{z,i}}{\partial z} \right] \\ \sigma_{kk} = \sigma_{xx} + \sigma_{yy} + \sigma_{zz} \end{array} \right.$$

2.1.2 Ice-sheet Evolution

The ice sheet evolution is represented by a parabolic polynomial equation, the ice thickness $\eta(x, t)$ at the location and time is shown as:

$$\eta(x, t) = H(t) \sqrt{1 - \left(\frac{x}{L(t)}\right)^2}$$

where $H(t)$ and $L(t)$ show maximum ice-sheet thickness and horizontal extension at time t .

For the base case glacial retreat scenario, we simulate a 30 ka glacial cycle with linear expansion and retreat. From 0 ka to 19 ka, ice-sheet grows from 0 to 3 km thickness to 1300 km lateral extent. The ice-sheet thickness remains 3 km during glacial maximum for another 1 ka. After glacial maximum, the ice sheet retreat to 0 km in the next 10 ka.

The net estimation of Antarctic glacial retreat indicates that fast-flowing ice-sheet (>800 m/a) retreat 110 meters with per meter of ice thinning³³. Here, we keep the ice-sheet expansion phase unchanged but use different ice-sheet retreat rates to test the influence of grounding line retreat rates on basal water flux. We calculate the ice-sheet thinning rate as the mean ice sheet thickness change within 64 km to the grounding line. We show that our moderate retreat scenario has a comparable grounding line retreat and ice thinning rate to Thwaites Glacier (Extended Data Fig. 2). Fast glacier retreat rate has been modelled with glacier retreat over 500 km in 300 years at Thwaites Glacier (1,677 m/a)³⁹.

2.1.3 Hydrology modelling

The subglacial hydraulic head change is solved by the Darcy flow:

$$\frac{\partial}{\partial x} \left[\frac{\rho_0 g}{\mu_f} \left(k_x \frac{\partial h}{\partial x} \right) \right] + \frac{\partial}{\partial z} \left[\frac{\rho_0 g}{\mu_f} \left(k_z \frac{\partial h}{\partial z} \right) \right] = S_s \frac{\partial h}{\partial t} - \rho_r k_z \frac{\rho_0 g}{\mu_f} - \frac{S_s B}{\rho_f g} \frac{\partial}{\partial t} \left(\frac{\sigma_{kk}}{3} \right)$$

where k_x and k_z represent the permeability of basal unit in the horizontal and vertical directions, h is the hydraulic head to be solved, t is time, g is the gravitational acceleration, μ_f is fluid viscosity, ρ_0 is the reference fluid density, ρ_f is the fluid density, ρ_r is the relative density of fluid density to reference fluid density, σ_{kk} is the total normal stress due to ice-sheet loading. The Skempton's coefficient B controls the percentage of ice loading support by the pore fluid. Measurement of sandstone, shale, and carbonate has a Skempton's coefficient range from 0.58 - 1, 0.98 - 0.99, and

$0.73 - 1$ respectively¹⁰⁹. We use $B = 1$ which assume that all loading due to ice sheet is supported by the subsurface pore fluid. S_s is the specific storage. Details of model parameters are listed at Table S4.

2.2 Model setting and boundary conditions

In CVFEM_Rift2D, the geomechanical model is coupled with the hydrologic model through interpolation of total normal stress. We use a coarse model to solve the lithosphere deformation and stress change associated with ice-sheet loading and unloading. A fine hydrology grid is implemented to solve groundwater transportation (Fig. S17). Here, we assume that any upward water at the surface will transport into ice-sheet bed or subglacial till layer.

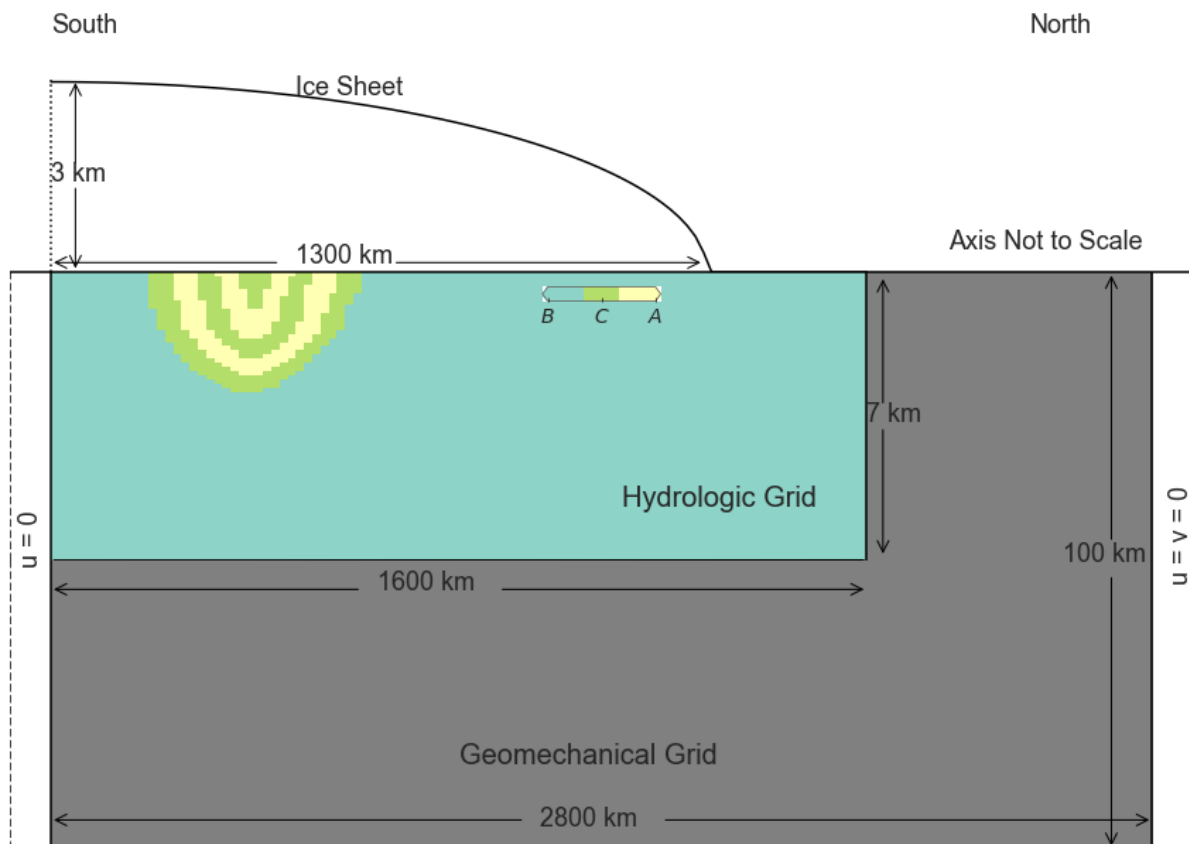


Fig. S17 Hydro-mechanical model setting. The ice-sheet over the top of sedimentary basin and basement (unit B) has a maximum extension of 1300 km and a maximum thickness of 3 km. Ice-sheet

flows from South to North. The sedimentary basin includes aquifer unit A and confine unit C. The sedimentary basin extends 400 km horizontally with a maximum depth of 3 km. We solve the groundwater flow and heat transportation at the top 7 km in the refined hydrologic grid. The geomechanical model is conducted in a coarser grid with a maximum extension of 100 km.

The geomechanical model extends 2800 km horizontally and 100 km vertically. There are 281 nodal columns and 11 nodal rows with 10 km intervals. We solve the geomechanical deformation with a time interval of 100 years.

In the geomechanical model, we set the north end as a non-displacement boundary condition for horizontal and vertical directions. For the south end boundary, we keep the no horizontal displacement boundary condition unchanged but release the constraint to allow vertical displacement. We assign the weight of ice-sheet as the top stress boundary of the model domain and solve beam bending equation to the bottom displacement boundary condition.

We assume a flat topography surface in the hydrologic model domain. The sedimentary basin is 400 km long, sitting on the top of the basement with a maximum depth of 3 km. The lithology in the sedimentary basin includes two basal aquifer units confined by the three aquitard units. We limit the hydrologic model domain to the top 7 km, as the free liquid phase water that connects to the land surface only exists in the upper portion of crust. The fine-sized hydrology grid has a horizontal interval of 16 km and a vertical interval of 0.1 km. It gives the hydrologic model domain with 101 nodal columns and 71 nodal rows. We use a 10 year time interval to solve the groundwater flow.

For the hydrological model domain, no flux boundaries are used for the bottom and sides boundaries. We specify the 90% of ice sheet thickness as the top hydraulic boundary conditions, where ice-sheet is at floating conditions:

$$h_{BC}(x, t) = 0.9\eta(x, t)$$

For the heat transformation, the initial temperature at the ice-sheet sole is set to 0°. We assume insulated side boundaries, and the basal heat flux condition is assigned at 60 mW m⁻².

Permafrost generally acts as a barrier to the groundwater flow^{32,110}. In our simulation, we ignore the impact of permafrost on groundwater transportation as a sedimentary basin located at the upper stream with thick ice. A wet base glacier assumption is valid in these thick ice cover areas.

2.3 Discussion

2.3.1 Impact of permeability to basal water flux

Our simulation delineates complex groundwater flow patterns and responses to external loading changes controlled by the permeability of the basal aquifer unit (Fig S18). For a normal (vertical permeability $\kappa_z = 10^{-15}$ m²) to low permeability case ($\kappa_z < 10^{-16}$ m²), the expansion of ice-sheet causes the basal water to recharge into sedimentary basin. In turn, the retreat of ice-sheet releases the loading to cause major water discharge into the basal water system.

A higher permeable basal aquifer ($\kappa_z \geq 10^{-14}$) facility groundwater transportation. Hence, it quickly adjusts the ice loading change through groundwater transportation (Supplement Video 2). In this case, water flows into the sedimentary basin (negative vertical water flux in Fig. 18a) at the upstream and discharges into the downstream region (positive vertical water flux in Fig. 18a) during ice-sheet expansion. The retreat of the ice-sheet causes a reduction of recharging water rate at the upstream of the sedimentary basin, and an enhancement of water discharge at the downstream side (Fig. 18b). This leads to an enhancement of water flux in the basal water system. Once the ice-sheet margin retreats over the top of the sedimentary basin, we see a dominant effect of enhanced water recharge at the up portion of sedimentary basin. The major part of water is transported into the groundwater system and discharged into the ice-free land.

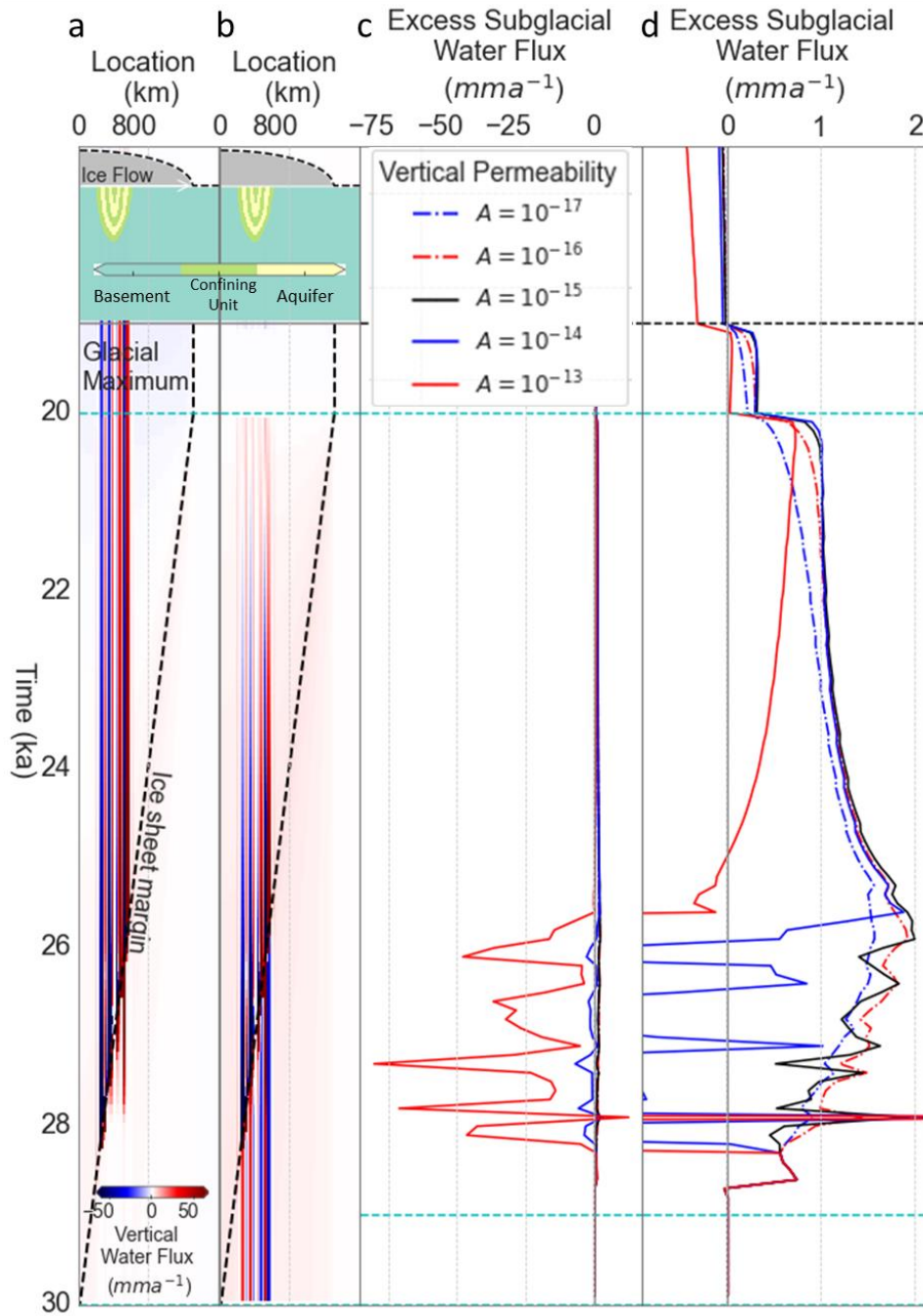


Fig. S18: Impact of permeability to basal water flux. **a**, Surface vertical water flux with $\kappa_z = 10^{13} m^2$. The upper stream portion of sedimentary basin shows water recharge, and the lower portion of sedimentary basin shows water discharge. **b**, Relative surface water flux change compares with the glacial maximum. At the initial ice sheet retreat phase, the positive water flux change indicates the reduction of water recharge and enhancement of water discharge. The following stage shows enhancement of both water discharge and recharge. **c**, Excess subglacial water flux (compare with

basement only case) with different permeability of aquifer units. **d**, A zoomed-in version of excess subglacial water flux change.

Although our simulation indicates groundwater flow patterns vary with the basal aquifer permeability, we observe a similar pattern of total water flux at the basal system at the first stage of ice-sheet retreat. Before the ice-sheet margin retreats over the sedimentary basin, the subglacial water flux is enhanced by a more permeable basal unit. The excess subglacial discharge rate (ESDR) changed from 1.5 mm a^{-1} to 2 mm a^{-1} , with the vertical permeability changing from 10^{-17} m^2 to 10^{-13} m^2 . The following phase shows different subglacial water flux controlled by permeability. A lower to normal permeable aquifer supports water discharge with a positive subglacial total water flux. The high permeable aquifer shows a complex subglacial total water flux pattern, with major water transformation through the groundwater system. This phenomenon is supported by the extremely low erosion rate at limestone¹¹¹, where major water is transported into the Karst limestone system. However, this case is not a common situation in Antarctica, due to the large compaction effect of ice-sheet. This could also refer to the case of freshwater discharge on the continental shelf¹¹².

2.3.2 Impact of sedimentary basin thickness to basal water flux

The sedimentary basin thickness also influences the amplitude of basal water flux (Fig. S19). We find an enhancement of basal water flux with a thicker sedimentary basin. For a 1 km thick sedimentary basin, subglacial water flux is enhanced by 0.4 mm a^{-1} . A 4.5 km thick sedimentary basin could enhance the mean basal water flux by 3 mm a^{-1} . The sedimentary basin thickness modelled by potential field data could be up to 8 km in Wilkes Subglacial Basin and Aurora Subglacial Basin^{15,79}. These widely distributed thick sedimentary basins indicate a potential groundwater influence on the ice dynamics in East Antarctica²⁶.

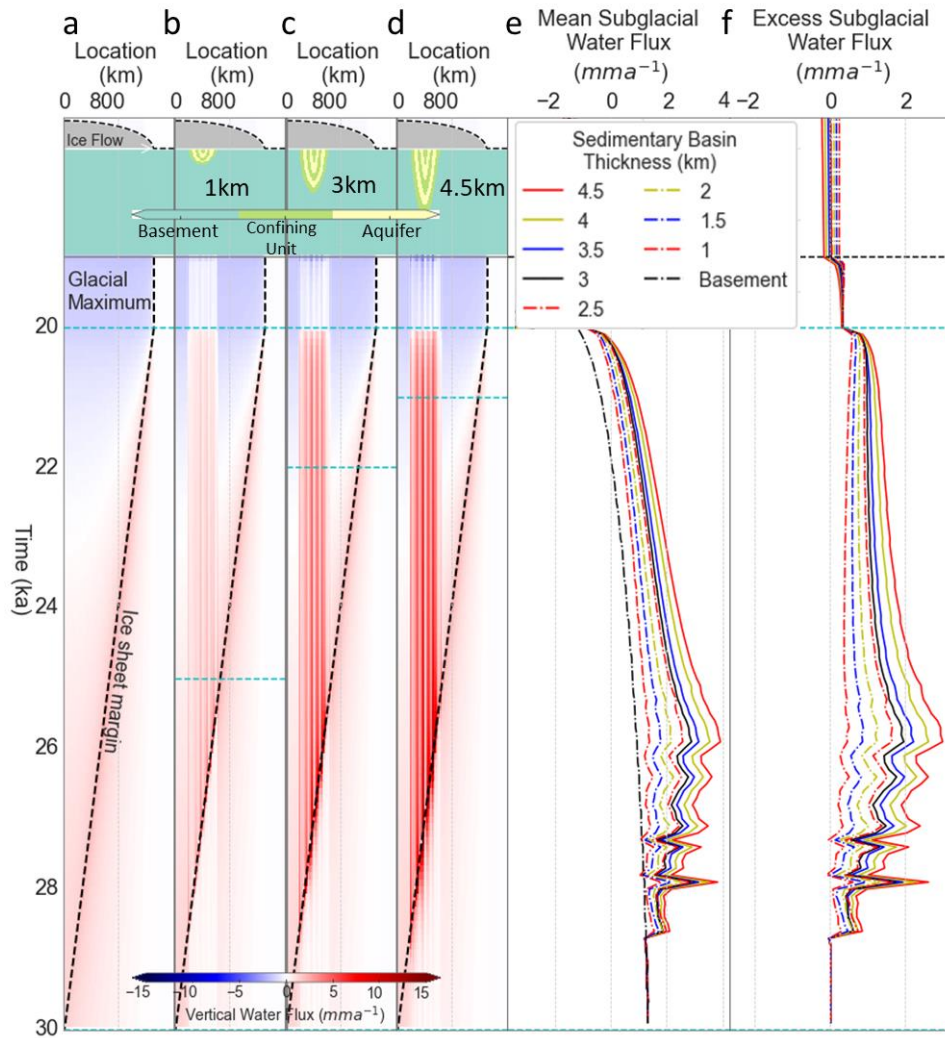


Fig. S19: Impact of sedimentary basin thickness on basal water flux. **a-d**, Surface vertical water flux change with sedimentary basin thickness. **a**, basement. **b**, 1 km sedimentary basin. **c**, 3 km sedimentary basin. **d**, 4.5 km sedimentary basin. **e**, Mean subglacial water flux change with different thicknesses of sedimentary basin. We see an enhancement of basal water flux with a thicker sedimentary basin. **f**, The excess subglacial water flux compare with the basement only case.

2.3.3 Impact of basal heat flux due to water transportation

We further test the impact of groundwater transportation on basal heat flux (Fig. S20). The ice-sheet expansion drives basal water recharge into the sedimentary basin. We observe a decrease in basal heat flux compared with the basement only region. During ice-sheet retreat, the surface heat flux is enhanced associated with the water discharge. For a 130 m a^{-1} retreat case, the surface heat flux is

enhanced by 1 mW m^{-2} compared with the glacial maximum. A faster retreat mode could enhance the basal heat flux by 5 mW m^{-2} .

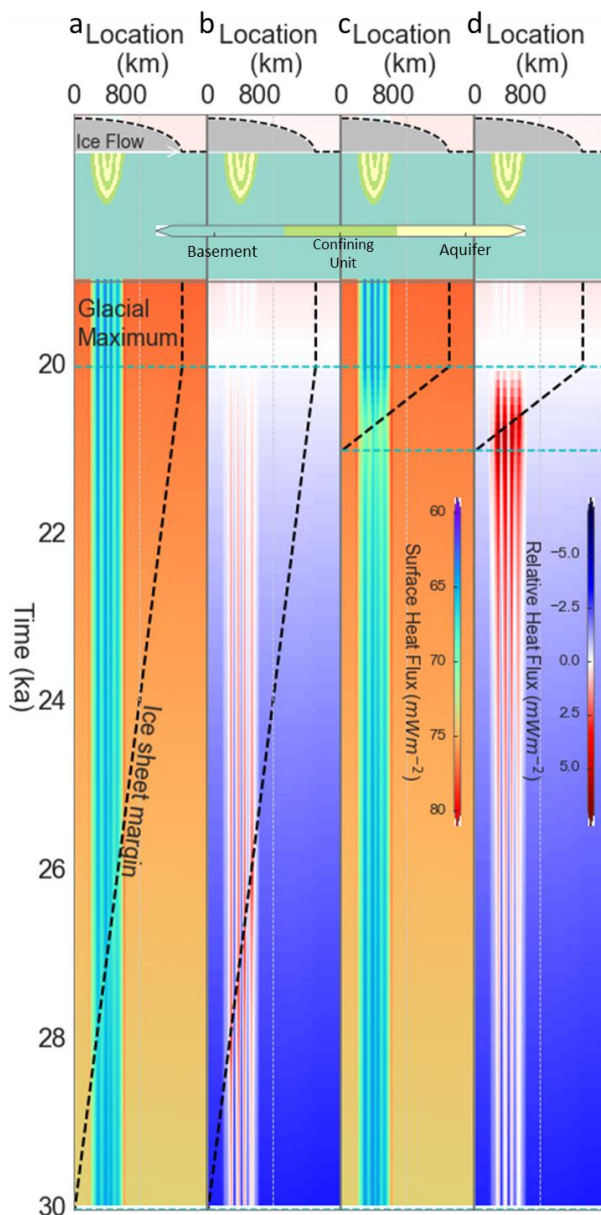


Fig. S20: Impact of ice sheet retreat on basal heat flux. **a**, Surface heat flux with a 130 m a^{-1} ice sheet retreat rate. **b**, relative surface heat flux compared with the glacial maximum with a 130 m a^{-1} ice sheet retreat rate. **c**, Surface heat flux with a $1,300 \text{ m a}^{-1}$ ice sheet retreat rate. **d**, relative surface heat flux compared with the glacial maximum with a $1,300 \text{ m a}^{-1}$ ice sheet retreat rate.

Supplement reference

- 55 Cox S.C., B., S. L. & team, T. G. (ed GNS Science) (GNS Science, Lower Hutt, New Zealand., 2019).
- 56 Jordan, T. A. *et al.* Inland extent of the Weddell Sea Rift imaged by new aerogeophysical data. *Tectonophysics* **585**, 137-160, doi:10.1016/j.tecto.2012.09.010 (2013).
- 57 Trey, H. *et al.* Transect across the West Antarctic rift system in the Ross Sea, Antarctica. *Tectonophysics* **301**, 61-74, doi:10.1016/s0040-1951(98)00155-3 (1999).
- 58 Hübscher, C., Jokat, W. & Miller, H. Structure and origin of southern Weddell Sea crust: results and implications. *Geol. Soc. Spec. Pub.* **108**, 201-211 (1996).
- 59 Straume, E. O. *et al.* GlobSed: Updated Total Sediment Thickness in the World's Oceans. *Geochem. Geophys. Geosyst.* **20**, 1756– 1772, doi:10.1029/2018gc008115 (2019).
- 60 Lowe, A. L. & Anderson, J. B. Reconstruction of the West Antarctic ice sheet in Pine Island Bay during the Last Glacial Maximum and its subsequent retreat history. *Quat. Sci. Rev.* **21**, 1879-1897 (2002).
- 61 Nitsche, F. O. *et al.* Paleo ice flow and subglacial meltwater dynamics in Pine Island Bay, West Antarctica. *The Cryosphere* **7**, 249-262 (2013).
- 62 Gohl, K., Denk, A., Eagles, G. & Wobbe, F. Deciphering tectonic phases of the Amundsen Sea Embayment shelf, West Antarctica, from a magnetic anomaly grid. *Tectonophysics* **585**, 113-123 (2013).
- 63 Karner, G. D., Studinger, M. & Bell, R. E. Gravity anomalies of sedimentary basins and their mechanical implications: Application to the Ross Sea basins, West Antarctica. *Earth Planet. Sci. Lett.* **235**, 577-596 (2005).
- 64 Anandakrishnan, S., Blankenship, D., Alley, R. & Stoffa, P. Influence of subglacial geology on the position of a West Antarctic ice stream from seismic observations. *Nature* **394**, 62-65 (1998).
- 65 Peters, L. E. *et al.* Subglacial sediments as a control on the onset and location of two Siple Coast ice streams, West Antarctica. *J. Geophys. Res. Solid Earth* **111** (2006).
- 66 Filina, I. Y. *et al.* New 3D bathymetry and sediment distribution in Lake Vostok: Implication for pre-glacial origin and numerical modeling of the internal processes within the lake. *Earth Planet. Sci. Lett.* **276**, 106-114, doi:10.1016/j.epsl.2008.09.012 (2008).
- 67 Chaput, J. *et al.* The crustal thickness of West Antarctica. *J. Geophys. Res. Solid Earth* **119**, 378-395 (2014).
- 68 Anandakrishnan, S. & Winberry, J. P. Antarctic subglacial sedimentary layer thickness from receiver function analysis. *Global Planet. Change* **42**, 167-176, doi:10.1016/j.gloplacha.2003.10.005 (2004).
- 69 Dunham, C. *et al.* A joint inversion of receiver function and Rayleigh wave phase velocity dispersion data to estimate crustal structure in West Antarctica. *Geophys. J. Int.* **223**, 1644-1657 (2020).
- 70 Piana Agostinetti, N., Roselli, P., Cattaneo, M. & Amato, A. Moho-depth and subglacial sedimentary layer thickness in the Wilkes Basin from receiver function analysis. *IASPEI-General Assembly* (2005).
- 71 Chai, C., Ammon, C. J., Anandakrishnan, S., Ramirez, C. & Nyblade, A. Estimating subglacial structure using P-wave receiver functions. *Geophys. J. Int.* **209**, 1064-1079, doi:10.1093/gji/ggx075 (2017).
- 72 Yan, P. *et al.* Antarctic ice sheet thickness estimation using the horizontal-to-vertical spectral ratio method with single-station seismic ambient noise. *The Cryosphere* **12**, 795-810, doi:10.5194/tc-12-795-2018 (2018).
- 73 Gupta, S., Kanna, N. & Akilan, A. Volcanic passive continental margin beneath Maitri station in central DML, East Antarctica: constraints from crustal shear velocity through receiver function modelling. *Polar Res.* **36**, 1332947 (2017).

- 74 Studinger, M. *et al.* Subglacial sediments: A regional geological template for ice flow in West Antarctica. **28**, 3493-3496, doi:10.1029/2000gl011788 (2001).
- 75 Bell, R. E., Studinger, M., Karner, G., Finn, C. A. & Blankenship, D. D. in *Antarctica* 117-121 (Springer, 2006).
- 76 Bamber, J. L. *et al.* East Antarctic ice stream tributary underlain by major sedimentary basin. *Geology* **34**, 33, doi:10.1130/g22160.1 (2006).
- 77 Aitken, A. R. *et al.* The subglacial geology of Wilkes Land, East Antarctica. *Geophys. Res. Lett.* **41**, 2390-2400, doi:10.1002/2014GL059405 (2014).
- 78 Ferraccioli, F., Armadillo, E., Jordan, T., Bozzo, E. & Corr, H. Aeromagnetic exploration over the East Antarctic Ice Sheet: A new view of the Wilkes Subglacial Basin. *Tectonophysics* **478**, 62-77, doi:10.1016/j.tecto.2009.03.013 (2009).
- 79 Frederick, B. C. *et al.* Distribution of subglacial sediments across the Wilkes Subglacial Basin, East Antarctica. *Journal of Geophysical Research: Earth Surface* **121**, 790-813, doi:<https://doi.org/10.1002/2015JF003760> (2016).
- 80 Paxman, G. J. *et al.* Subglacial Geology and Geomorphology of the Pensacola-Pole Basin, East Antarctica. *Geochemistry Geophysics Geosystems* **20**, doi:10.1029/2018GC008126 (2019).
- 81 Maritati, A. *et al.* The tectonic development and erosion of the Knox Subglacial Sedimentary Basin, East Antarctica. *Geophys. Res. Lett.* **43**, 10,728-10,737, doi:10.1002/2016gl071063 (2016).
- 82 Paxman, G. J. *et al.* Reconstructions of Antarctic topography since the Eocene–Oligocene boundary. *Palaeogeography, palaeoclimatology, palaeoecology* **535**, 109346 (2019).
- 83 Shepard, M. K. *et al.* The roughness of natural terrain: A planetary and remote sensing perspective. *Journal of Geophysical Research: Planets* **106**, 32777-32795 (2001).
- 84 Young, D. A., Richter, T. G., Powell, E. M., Quartini, E. & Blankenship, D. D. (U.S. Antarctic Program (USAP) Data Center, 2017).
- 85 Tinto, K. J. *et al.* Ross Ice Shelf response to climate driven by the tectonic imprint on seafloor bathymetry. *Nat. Geosci.*, doi:10.1038/s41561-019-0370-2 (2019).
- 86 Forsberg, R. *et al.* Exploring the Recovery Lakes region and interior Dronning Maud Land, East Antarctica, with airborne gravity, magnetic and radar measurements. *Geol. Soc. Spec. Pub.* **461**, 23-34 (2018).
- 87 Sandwell, D. T., Muller, R. D., Smith, W. H. F., Garcia, E. & Francis, R. New global marine gravity model from CryoSat-2 and Jason-1 reveals buried tectonic structure. **346**, 65-67, doi:10.1126/science.1258213 (2014).
- 88 Kvas, A. *et al.* (ed GFZ Data Services) (2019).
- 89 Uieda, L., Barbosa, V. C. F. & Braatenberg, C. Tesseroids: Forward-modeling gravitational fields in spherical coordinates. **81**, F41-F48, doi:10.1190/geo2015-0204.1 (2016).
- 90 An, M. *et al.* S-velocity model and inferred Moho topography beneath the Antarctic Plate from Rayleigh waves. *J. Geophys. Res. Solid Earth* **120**, 359-383, doi:10.1002/2014jb011332 (2015).
- 91 Pappa, F., Ebbing, J. & Ferraccioli, F. Moho Depths of Antarctica: Comparison of Seismic, Gravity, and Isostatic Results. *Geochem. Geophys. Geosyst.*, doi:10.1029/2018gc008111 (2019).
- 92 Ebbing, J. *et al.* Earth tectonics as seen by GOCE - Enhanced satellite gravity gradient imaging. *Sci Rep* **8**, 16356, doi:10.1038/s41598-018-34733-9 (2018).
- 93 Arkani-Hamed, J. Differential reduction to the pole: Revisited. *Geophysics* **72**, L13-L20, doi:10.1190/1.2399370 (2006).
- 94 Melo, F. F., Gonzalez, S. P., Barbosa, V. C. & Oliveira Jr, V. C. Amplitude of the magnetic anomaly vector in the interpretation of total-field anomaly at low magnetic latitudes. *J. Appl. Geophys.* **190**, 104339 (2021).

- 95 Guo, L., Meng, X. & Zhang, G. Three-dimensional correlation imaging for total amplitude magnetic anomaly and normalized source strength in the presence of strong remanent magnetization. *J. Appl. Geophys.* **111**, 121-128 (2014).
- 96 Salem, A. *et al.* Mapping the depth to magnetic basement using inversion of pseudogravity: Application to the Bishop model and the Stord Basin, northern North Sea. *Interpretation* **2**, T69-T78, doi:10.1190/int-2013-0105.1 (2014).
- 97 Martos, Y. M. *et al.* Heat Flux Distribution of Antarctica Unveiled. *Geophys. Res. Lett.* **44**, 11,417-411,426, doi:10.1002/2017gl075609 (2017).
- 98 Morlighem, M., Seroussi, H., Larour, E. & Rignot, E. Inversion of basal friction in Antarctica using exact and incomplete adjoints of a higher-order model. *118*, 1746-1753, doi:10.1002/jgrf.20125 (2013).
- 99 Diesing, M. Deep-sea sediments of the global ocean. *Earth System Science Data* **12**, 3367-3381 (2020).
- 100 Kursa, M. B. & Rudnicki, W. R. Feature selection with the Boruta package. *J Stat Softw* **36**, 1-13 (2010).
- 101 Reshef, D. N. *et al.* Detecting novel associations in large data sets. *Science* **334**, 1518-1524 (2011).
- 102 Albanese, D. *et al.* Minerva and minepy: a C engine for the MINE suite and its R, Python and MATLAB wrappers. *Bioinformatics* **29**, 407-408 (2013).
- 103 Strobl, C., Boulesteix, A.-L., Zeileis, A. & Hothorn, T. Bias in random forest variable importance measures: Illustrations, sources and a solution. *BMC bioinformatics* **8**, 25 (2007).
- 104 Valavi, R., Elith, J., Lahoz-Monfort, J. J. & Guillera-Arroita, G. block CV: An r package for generating spatially or environmentally separated folds for k-fold cross-validation of species distribution models. *Methods in Ecology and Evolution* **10**, 225-232 (2019).
- 105 Burton-Johnson, A. & Riley, T. Autochthonous v. accreted terrane development of continental margins: a revised in situ tectonic history of the Antarctic Peninsula. *J. Geol. Soc.* **172**, 822-835 (2015).
- 106 Young, D. A. *et al.* A dynamic early East Antarctic Ice Sheet suggested by ice-covered fjord landscapes. *Nature* **474**, 72-75 (2011).
- 107 Blankenship, D. D. *et al.* Active volcanism beneath the West Antarctic ice sheet and implications for ice-sheet stability. *Nature* **361**, 526-529 (1993).
- 108 Eagles, G. *et al.* Erosion at extended continental margins: Insights from new aerogeophysical data in eastern Dronning Maud Land. *Gondwana Res.* **63**, 105-116, doi:10.1016/j.gr.2018.05.011 (2018).
- 109 Green, D. H. & Wang, H. F. Fluid pressure response to undrained compression in saturated sedimentary rock. *Geophysics* **51**, 948-956 (1986).
- 110 Lemieux, J. M., Sudicky, E., Peltier, W. & Tarasov, L. Dynamics of groundwater recharge and seepage over the Canadian landscape during the Wisconsinian glaciation. *J. Geophys. Res. Earth Surface* **113** (2008).
- 111 Steinemann, O. *et al.* Quantifying glacial erosion on a limestone bed and the relevance for landscape development in the Alps. *Earth Surf. Processes Landforms* **45**, 1401-1417 (2020).
- 112 DeFoer, W. *et al.* Ice sheet-derived submarine groundwater discharge on Greenland's continental shelf. *Water Resour. Res.* **47** (2011).

Supplement table

Table. S1 The sedimentary basin and basement distribution from seismic study.

<i>FID</i>	<i>Name</i>	<i>Latitude</i>	<i>Longitude</i>	<i>SSB_thickness</i>	<i>Source</i>	<i>Label</i>
0	ATOL	-71.3897	-68.8701	0	Dunham et al., 2020 ⁶⁹	Basement
1	BREN	-72.675	-63.021	0		Basement
2	BYRD	-80.017	-119.474	0		Basement
3	FOWL	-76.8928	-79.3011	0		Basement
4	HOWD	-77.5286	-86.7694	0		Basement
5	MA01	-76.9397	-97.5596	0		Basement
6	MA02	-77.4394	-97.5595	0.1		SSB
7	MA03	-77.9401	-97.5585	0		Basement
8	MA04	-78.4221	-97.5879	0.1		SSB
9	MA05	-78.9395	-97.5573	0		Basement
10	MA06	-79.4397	-97.5587	0.4		SSB
11	MA07	-78.2496	-93.4991	0.1		SSB
12	MA08	-77.4014	-103.002	0.8		SSB
13	MA09	-79.8993	-104.998	0		Basement
14	MA10	-78.5999	-109	0		Basement
15	MECK	-75.2808	-72.185	0		Basement
16	PIG1	-73.9782	-97.575	0		Basement
17	PIG2	-74.4557	-97.683	0.1		SSB
18	PIG3	-75.0841	-97.4744	0		Basement
19	PIG4	-75.7599	-97.583	0.2		SSB
20	ROTH	-67.52	-68.1488	0		Basement
21	STEW	-84.1863	-86.2349	0		Basement
22	THUR	-72.5301	-97.5606	0		Basement
23	UNGL	-79.7746	-82.524	0		Basement
24	UPTW	-77.5781	-109.037	0.3		SSB
25	WAIS	-79.4181	-111.778	0		Basement
26	WELC	-70.7318	-63.8274	0		Basement
27	WHIT	-82.6823	-104.387	0		Basement
28	WILS	-80.0396	-80.5587	0		Basement
29	ST01	-83.2279	-98.7419	0.2	Chaput et al.,2014 ⁶⁷	SSB
30	ST02	-82.069	-109.124	0.27		SSB
31	ST03	-81.4065	-113.15	0		Basement
32	ST04	-80.715	-116.578	0.35		SSB
33	ST06	-79.3316	-121.82	0.23		SSB
34	ST07	-78.6387	-123.795	0		Basement
35	ST08	-77.9576	-125.531	0.15		SSB
36	ST10	-75.8143	-129.749	0.3		SSB
37	ST12	-76.897	-123.816	0		Basement
38	ST14	-77.8378	-134.08	0		Basement
39	CLRK	-77.3231	-141.849	0		Basement
40	WNDY	-82.3695	-119.413	0		Basement
41	FALL	-85.3066	-143.628	0		Basement
42	SILY	-77.1332	-125.966	0		Basement

43	DNTW	-76.4571	-107.78	0		Basement
44	WHIT	-82.6823	-104.387	0		Basement
45	MPAT	-78.0297	-155.022	0		Basement
46	MECK	-75.2807	-72.1849	0		Basement
47	HOWD	-77.5285	-86.7694	0		Basement
48	WILS	-80.0396	-80.5587	0		Basement
49	DUFK	-82.8619	-53.2007	0		Basement
50	PECA	-85.6124	-68.5527	0		Basement
51	LONW	-81.3466	152.735	0		Basement
52	MILR	-83.3063	156.2517	0		Basement
53	SURP	-84.7199	-171.202	0		Basement
54	DEVL	-81.4757	161.9745	0		Basement
55	FISH	-78.9276	162.5652	0		Basement
56	WAIS	-79.4181	-111.778	0		Basement
57	BYRD	-80.0168	-119.473	0		Basement
58	THUR	-72.5301	-97.5606	0		Basement
59	UPTW	-77.5797	-109.04	0.3		SSB
60	ISDE	-80	-135	0	Anandakrishnan & Winberry, 2004 ⁶⁸	Basement
61	MBL	-78.0994	-130.229	0.26		SSB
62	MTM	-79.5044	-100.021	0.55		SSB
63	SDM	-81.6247	-148.85	0.3		SSB
64	OND	-80.7539	-125.738	0.25		SSB
65	STC2	-82.3625	-136.41	0		Basement
66	STC6	-82.4514	-136.428	0.18		SSB
67	N052	-79.5511	145.7592	0.3		SSB
68	JNCT	-76.9367	157.9019	0		Basement
69	SPA	-90	0	0.2		SSB
70	1	-71.6	159.5	0	Agostinetti et al., 2005 ⁷⁰	Basement
71	3	-71.7	156.8	0.25		SSB
72	4	-71.8	154.6	0.2		SSB
73	5	-71.9	152.5	0		Basement
74	Onset	-82.278	-121.555	0.4	Anandakrishnan et al., 1998 ⁶⁴	SSB
75	N060	-80	142.6	1	Yan et al., 2018 ⁷²	SSB
76	E028	-76.3075	154.0394	1	Chai et al., 2017 ⁷¹	SSB
77	Maitri	-70.76	11.73	1.5	Gupta et al., 2017 ⁷³	SSB

Table. S2 Confusion matrix of 10 sub_RF models. Validation (reference) classes are in columns; predicted classes are in row. Note, 5 SSB points are excluded during the spatial blocks assignment process.

Reference \ Prediction	Basement	SSB	Row Total	Error of commission
Basement	488	150	638	0.235
	SSB	120	458	578
	Column Total	608	608	sub_RF1
	Error of omission	0.197	0.247	
Basement	496	150	646	0.232
	SSB	112	457	569
	Column Total	608	607	sub_RF2
	Error of omission	0.184	0.247	
Basement	498	159	657	0.242
	SSB	110	448	558
	Column Total	608	607	sub_RF3
	Error of omission	0.181	0.262	
Basement	492	169	661	0.256
	SSB	116	439	555
	Column Total	608	608	sub_RF4
	Error of omission	0.191	0.278	
Basement	489	159	648	0.245
	SSB	119	449	568
	Column Total	608	608	sub_RF5
	Error of omission	0.196	0.262	
Basement	496	146	642	0.227
	SSB	112	461	573
	Column Total	608	607	sub_RF6
	Error of omission	0.184	0.241	
Basement	492	153	645	0.237
	SSB	116	454	570
	Column Total	608	607	sub_RF7
	Error of omission	0.191	0.252	
Basement	487	160	647	0.247
	SSB	121	448	569
	Column Total	608	608	sub_RF8
	Error of omission	0.199	0.263	
Basement	494	149	643	0.232
	SSB	114	458	572
	Column Total	608	607	sub_RF9

Error of omission	0.188	0.245		
Basement	493	142	635	0.224
SSB	115	466	581	0.198
Column Total	608	608		
Error of omission	0.189	0.234		sub_RF10
Basement	4925	1537	6462	0.238
SSB	1155	4538	5693	0.203
Column Total	6080	6075		
Error of omission	0.190	0.253		Total

Table. S3 Confusion matrix use all training points. Validation (reference) classes are in columns; predicted classes are in row.

Reference \ Prediction	Basement	SSB	Row Total	Error of commission
Basement	4957	1431	6388	0.224
SSB	1123	4648	5771	0.195
Column Total	6080	6079		
Error of omission	0.185	0.235		

Table. S4 Model Setting in Hydro-mechanical model

Property name	Value
Young's modulus of lithosphere (E)	56 GPa
Poisson ratio (ν)	0.25
Elastic thickness of lithosphere (L)	100 km
Flexural rigidity of lithosphere	$6.22 \times 10^{24} \text{ Pa}^*\text{m}^3$
Diffusivity of asthenosphere	$50 \text{ km}^2/\text{a}$
Mantle density (ρ_m)	$3,380 \text{ kg/m}^3$
Ice density (ρ_{ice})	900 kg/m^3
Gravitational constant (g)	9.812 m/s^2
Specific Storage (Ss)	10^{-6} m^{-1}
Bedrock permeability ($k_x = k_z; \text{ m}^2$)	10^{-19} m^2
Skempton constant (B)	1
Aquifer permeability ($k_x, k_z; \text{ m}^2$)	$10^{-14}, 10^{-15}$
Confining unit permeability ($k_x, k_z; \text{ m}^2$)	$10^{-16}, 10^{-17}$